

Absence of entanglement transition due to feedback-induced skin effect

Yu-Peng Wang,^{1,2} Chen Fang,^{1,3,4,*} and Jie Ren^{1,2,†}

¹*Beijing National Laboratory for Condensed Matter Physics and Institute of Physics, Chinese Academy of Sciences, Beijing 100190, China*

²*University of Chinese Academy of Sciences, Beijing 100049, China*

³*Songshan Lake Materials Laboratory, Dongguan, Guangdong 523808, China*

⁴*Kavli Institute for Theoretical Sciences, Chinese Academy of Sciences, Beijing 100190, China*

A quantum many-body system subject to unitary evolution and repeated local measurements with an increasing rate undergoes an entanglement transition from (sub)extensive to area law entropy scaling. We find that certain open boundary systems under “generalized monitoring”, consisting of “projective monitoring” and conditional feedback, display an anomalous late-time particle concentration on the edge, reminiscent of the “skin effect” in non-Hermitian systems. Such feedback-induced skin effect will suppress the entanglement generation, rendering the system short-range entangled without any entanglement transition.

The competition between the measurement and unitary evolution produces a novel *measurement-induced phase transition* (MIPT) [1–11], where a random quantum circuit [12–16] interspersed by onsite measurements with an increasing rate goes from a volume-law regime to an area-law regime. Similar entanglement transitions also appear in the context of monitored fermions [17–25], monitored open systems [26, 27], circuits with pure measurements [28, 29], random tensor networks [30–33], and quantum error correction thresholds [34–37]. Measurements introduce intrinsic randomness to the otherwise deterministic dynamics, with each set of recorded measurement results corresponding to a specific trajectory [38]. Among various frameworks trying to explain the MIPT [18, 25, 34–37, 39–46], one approach focuses on a specific trajectory, of which the evolution is described by a non-Hermitian Hamiltonian, where the entanglement transition in some systems coincides with the spontaneous *PT* symmetry breaking [47–51].

One unique phenomenon in certain non-Hermitian open boundary systems is the *non-Hermitian skin effect* [52–59], where a finite portion of the eigenstates are spatially concentrated on the edges. Dynamically, the skin effect implies that the late-time state from the quench dynamics will have particles concentrated near the edges. The Pauli exclusion principle predicts a nearly tensor-product structure of the steady state which obeys the area-law entanglement scaling, suggesting the absence of MIPT and seemingly contradicting the putative universal entanglement transition in the monitored systems. However, this simple argument assumes that the particular non-Hermitian evolution captures the entanglement behavior of the whole ensemble of trajectories, which is generally not guaranteed. Indeed, we will show in this work that for systems under “projective monitoring” (the exact definition of which will be given later), there will be

no skin effect in the trajectory-averaged dynamics. A natural question is whether the skin effect can appear in the whole ensemble of trajectories and thus suppress the entanglement transition.

In this letter, we answer the question positively by considering a generalized version of monitoring. The central result is the discovery of a feedback-induced skin effect (FISE) in the generalized monitored fermionic open boundary systems. We introduce an extensive local order parameter, the classical entropy, which not only characterizes the skin effect but also imposes an upper bound on the bipartite entanglement entropy. Numerical simulations of finite-size open boundary systems show a scale invariance of the classical entropy, which implies the saturation of the entanglement entropy in the thermodynamics limit at arbitrarily small measurement rates. The scaling property persists even when the interaction is turned on, therefore eliminating (sub)extensive entangled phases believed to appear in the weakly-monitored regime. Besides, FISE also gives a many-body version of the skin effect, which is numerically tractable due to the suppression of entanglement, and which, in principle, can be experimentally realized without exponential overheads.

Projective and generalized monitoring.— A standard quantum measurement process can be represented by a set of projectors P_m , each corresponding to a different measurement outcome. Measuring a state $|\psi\rangle$ yields a probability distribution over the possible outcomes, given by the Born rule: $p_m = \langle\psi|P_m|\psi\rangle$. The state then collapses to $P_m|\psi\rangle/\sqrt{p_m}$. When the unitary evolution is governed by a Hamiltonian, we can consider a coarse-grained version of the dynamics known as *projective monitoring*. This approach is formulated using the stochastic Schrödinger equation (SSE) [60–62]:

$$d|\psi\rangle = -i \left[H - \frac{i\gamma}{2} \sum_m (P_m - \langle\psi|P_m|\psi\rangle) \right] |\psi\rangle dt + \sum_m \left[\frac{P_m|\psi\rangle}{\|P_m|\psi\rangle\|} - |\psi\rangle \right] dW_m, \quad (1)$$

* cfang@iphy.ac.cn

† jieren@iphy.ac.cn

where each dW_m is an independent Poisson random variable taking the values 0 or 1. In a small time interval Δt , the probability of observing $dW_m = 1$ (i.e., the probe registers a quantum jump) is proportional to $\gamma\Delta t$. If $dW_m = 0$ for all m (the no-click limit) [38, 61], the evolution is described by an effective non-Hermitian Hamiltonian $H_{\text{eff}} = H - i\gamma/2 \sum_m P_m$. However, the no-click limit requires exponentially many experiments to be carried out before a desired trajectory is obtained.

The dynamics described by Eq. (1) can also be formulated in the density matrix formalism using the Lindblad master equation [63–65]:

$$\frac{d}{dt}\rho = -i[H, \rho] - \frac{\gamma}{2} \sum_m \{L_m^\dagger L_m, \rho\} + \gamma \sum_m L_m \rho L_m^\dagger, \quad (2)$$

where $\overline{|\psi\rangle\langle\psi|}$ is the density matrix averaged over all trajectories, and $L_m = P_m$ is referred to as the *jump operator*. The Lindblad equation in general yields a unique steady state ρ_{NESS} , characterized by $\frac{d}{dt}\rho_{\text{NESS}} = 0$ and $\text{Tr}[n_i \rho_{\text{NESS}}] = \nu$ (where ν is the filling number). We prove the uniqueness of the steady state ρ_{NESS} for the specific model considered in this work in the Supplemental Materials (SM) [66].

It is important to note that projective monitoring is an idealized representation of an actual measurement process. In practice, detecting a quantum state requires a probe to interact with the system, which inevitably disturbs the measured states. The more general form of a quantum measurement is described by the *positive operator-valued measure* (POVM) formalism [67, 68]. A continuous version of the POVM, called the generalized monitoring, is formulated as the stochastic Schrödinger equation (SSE) in Eq. (1), with the projector P_m replaced by a general operator L_m . In this study, we focus on a particular form of SSE where $L_m = U_m P_m$, corresponding to adding a unitary feedback operator U_m to the projective monitoring process. The conditional feedback does not affect the effective non-Hermitian Hamiltonian H_{eff} , but instead operates on those trajectories that deviated from the post-selected trajectory.

Feedback-induced skin effect. — We consider a spinless fermion chain described by a nearest-neighbor hopping Hamiltonian:

$$H = \sum_i (c_i^\dagger c_{i+1} + c_{i+1}^\dagger c_i). \quad (3)$$

The observable of interest in this system is the occupation number of a local quasimode created by a two-site projector

$$P_i = d^\dagger d, \quad \text{where } d = \frac{1}{\sqrt{2}}(c_i + ic_{i+1}). \quad (4)$$

The quasimode is a right-moving wave packet, which can be expressed as $d^\dagger = \sum_k f(k) c_k^\dagger$ in momentum space, where $|f(k)|^2 = \frac{1}{4}(1 + \sin k)$. The effective non-Hermitian

Hamiltonian for the monitored system is given by

$$H_{\text{eff}} = \sum_i \left[t_L c_i^\dagger c_{i+1} + t_R c_{i+1}^\dagger c_i - \mu(n_i + n_{i+1}) \right], \quad (5)$$

where $t_{L/R} = 1 \pm \gamma/4$ and $\mu = i\gamma/4$. This Hamiltonian is known as the Hatano-Nelson model [69] and displays the non-Hermitian skin effect. The post-selected evolution corresponds to the trajectory where no such mode is detected, leaving the left-moving mode probabilistically favored. In the projective monitoring case, the detected right-moving quasimodes will balance out the momentum distribution, leaving a steady state of homogeneity. See SM [66] for the numerical details.

However, successful detection in the monitored dynamics followed by a single-site θ -phase rotation

$$U_i = \exp(i\theta n_{i+1}) \quad (6)$$

(we will focus on the $\theta = \pi$ case) converts the detected d^\dagger mode to a left-moving quasimode

$$\tilde{d}^\dagger \equiv U d^\dagger U^\dagger = \frac{1}{\sqrt{2}}(c_i^\dagger + ic_{i+1}^\dagger). \quad (7)$$

Consequently, the monitored dynamics with feedback always increase left-moving particles, resulting in the FISE where particles concentrate on the left boundary. Specifically, for an open boundary system starting from the half-filled product state $|\psi_0\rangle = |1 \cdots 10 \cdots 0\rangle$, the late-time dynamics still feature two static domains where $\langle n_i \rangle$ only takes the extreme value of 1 or 0 (left panel of Fig. 1a). The particle diffusion happens only in the vicinity of the border, where the discontinuous particle density blurs to a “domain-wall region”. Comparing this with the dynamics with the periodic boundary conditions (right panel of Fig. 1a), where particles quickly disperse into a homogeneous state, we see the FISE features an anomalous boundary sensitivity.

We introduce the classical entropy as a local order parameter to characterize particle localization:

$$S_{\text{cl}}[\{n_i\}] \equiv - \sum_i [n_i \log n_i + (1 - n_i) \log(1 - n_i)]. \quad (8)$$

where only the nontrivial density (i.e., $n_i \neq 0, 1$) contributes to S_{cl} . In Fig. 1a, we show the time evolution of the classical entropies $S_{\text{cl}}[\{\langle n_i \rangle\}]$ starting from $|\psi_0\rangle$ under open boundary conditions. The numerical simulations support the “domain-wall developing” picture, where the evolution of $S_{\text{cl}}(t)$ follows a universal pattern when considering a system larger than the size of the domain-wall region (denoted as L_{DW}):

$$S_{\text{cl}}(\gamma, t, L > L_{\text{DW}}) = \frac{1}{\gamma} f(\gamma t), \quad (9)$$

where the system reaches the steady state with a characteristic relaxation time $t_{\text{rx}} \sim \gamma^{-1}$.

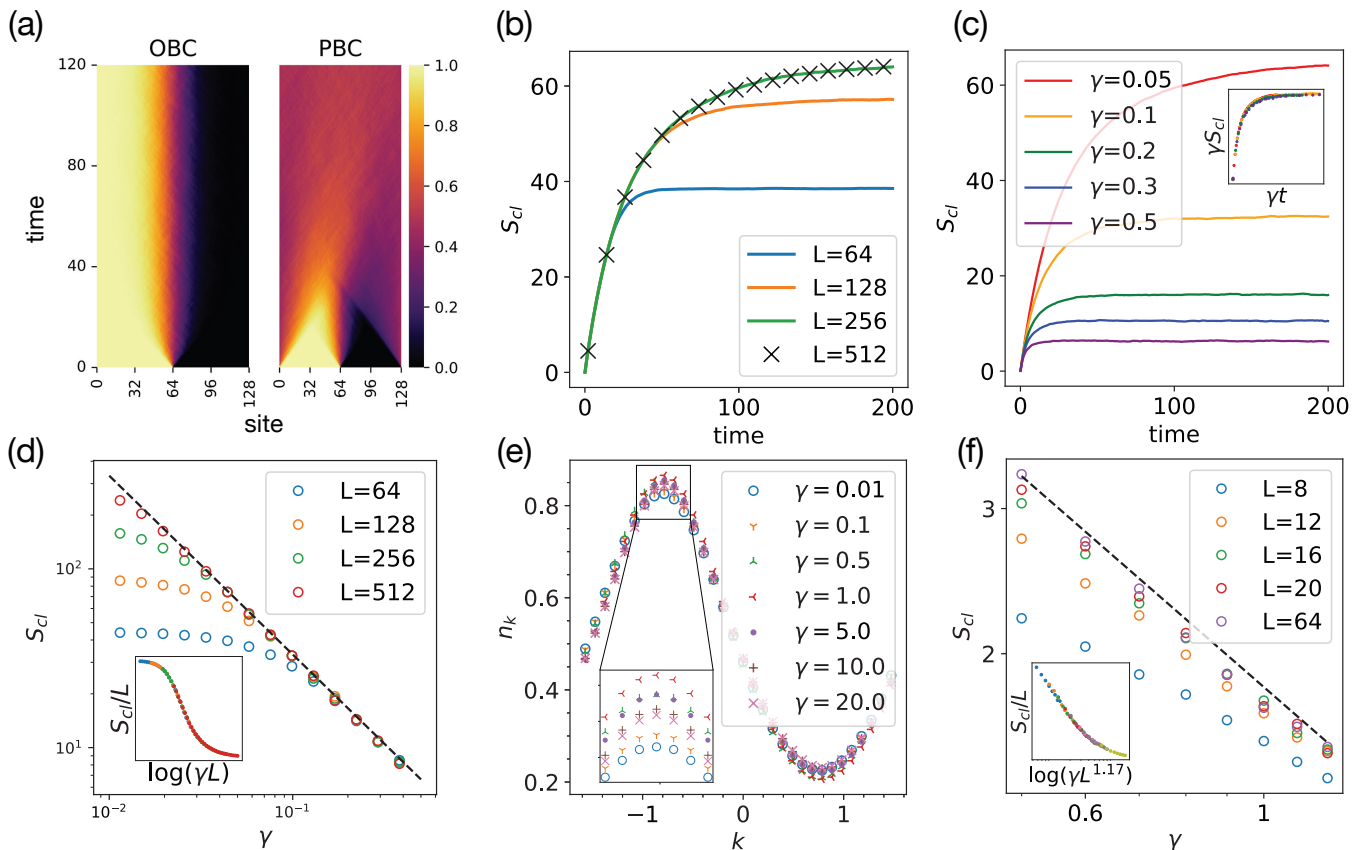


FIG. 1. (a) Mean particle density evolutions of generalized monitored free fermions ($L = 128$, $\gamma = 0.1$) under open boundary conditions (OBC) and periodic boundary conditions (PBC). The feedback induces a strong boundary sensitivity: under OBC the particle density evolves to be evenly distributed, while under PBC the steady state still features the domain structure. (b) Mean dynamics of S_{cl} for $\gamma = 0.05$ for different system sizes. The final saturation values of S_{cl} depend on the system size L when L is no bigger than the domain wall length L_{DW} . While for sufficiently large size ($L \geq 256$ in this case), $S_{cl}(t)$ shows no system size dependence. (c) Mean dynamics of S_{cl} for $L = 512$ ($L > L_{DW}$ for all γ 's we choose). The data collapse indicates that the saturated evolution $S_{cl}(t; L > L_{DW})$ fits into the universal form Eq. (9). (d) Finite size scaling of steady-state S_{cl} , which approach the line $S_{cl} = c/\gamma$ where $c \approx 3.3$. Inset: data collapse indicates the scaling form Eq. (10). (e) Momentum distribution of the steady state, in the periodic boundary conditions. (f) Steady-state S_{cl} for interacting monitored model, which approach the line $S_{cl} = c'/\gamma^{0.85}$ where $c' \approx 1.8$. The data collapse indicates that the universal scaling form is the same as the free fermion case.

Furthermore, we observe that the steady-state S_{cl} has a scale invariance, as shown in Fig. 1b:

$$S_{cl}(\gamma, t > t_{\text{rlx}}, L) = Lg(\gamma L), \quad (10)$$

which implies that $L_{DW} \sim \gamma^{-1}$. In the late-time and thermodynamics limit, the asymptotic behaviors of the scaling functions are $f(x \rightarrow \infty) \sim c$, $g(x \rightarrow \infty) \sim c/x$, where c is a numerical constant estimated to be 3.3 in this specific case. Therefore,

$$S_{cl}(\gamma, t > t_{\text{rlx}}, L > L_{DW}) = \frac{c}{\gamma} \approx \frac{3.3}{\gamma}. \quad (11)$$

Notably, Equation (10) suggests a scale invariance for the steady-state density profile $n(x)$ in the continuum limit [70]. The finite value of S_{cl} implies that the feedback-induced skin effect is present even for a vanishingly small measuring rate.

The skin effect also manifests as a directional bulk current in the periodic boundary systems. By simulating the system with identical parameters but under periodic boundary conditions, we show in Fig. 1d that there is an imbalance in the momentum distribution even for the $\gamma \ll 1$ case. We can characterize such imbalance by the current

$$J[n_k] \equiv \int_{-\pi}^{+\pi} v_k n_k dk, \quad (12)$$

where in the $\gamma \ll 1$ limit, we can approximate the velocity by the dispersion of free Hamiltonian: $v_k \simeq \partial_k E(k) = \sin(k)$. For $\gamma = 0.01$ case, $J \approx -0.94$. The nonzero current suggests the skin effect under open boundary condition.

Suppression of entanglement.— One of the consequences of FISE is the suppression of entanglement.

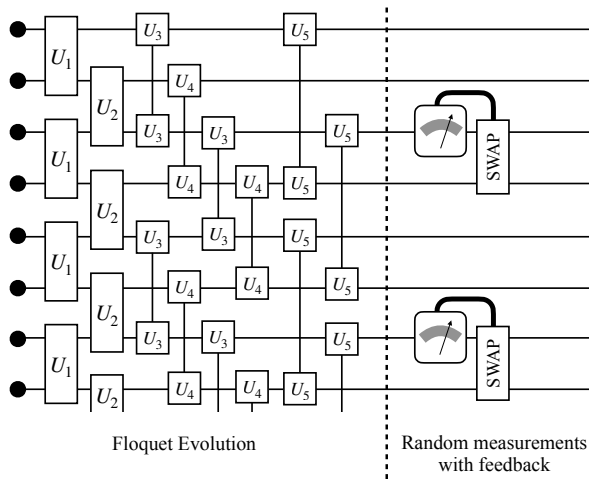


FIG. 2. Quantum circuit diagram suitable for the trapped-ion systems. The quantum gate U_1, \dots, U_5 are some combinations of $XX(\theta)$, $YY(\theta)$, and $XY(\theta)$ gates. The random measurements read out S_i^z values.

Specifically, we prove that S_{cl} imposes an upper bound for the (trajectory-averaged) steady-state entropy of the monitored dynamics. Consider an arbitrary subsystem A inside the monitored system. The entanglement *sub-additivity* [67, 68] leads to the inequality $S_A \leq \sum_i S_i$. Further, since the eigenvalues of a positive 2×2 matrix majorize [71] the diagonal elements, and thus have less entropy, $S_i \leq n_i \log n_i + (1 - n_i) \log(1 - n_i)$, and thus $S_A \leq S_{\text{cl}}[\{n_i \in A\}]$. For a pur state, $S_A = S_{\bar{A}}$, $S_A + S_{\bar{A}} = S_{\text{cl}}[\{n_i\}]$, therefore $S_A \leq S_{\text{cl}}/2$. Since the entropy function is convex, the trajectory averaging will be bounded:

$$\overline{S_A} \leq \frac{1}{2} \overline{S_{\text{cl}}[\{\langle n_i \rangle\}]} \leq \frac{1}{2} S_{\text{cl}}[\langle n_i \rangle]. \quad (13)$$

The asymptotic behavior, therefore, predicts the area-law entanglement scaling $S \leq c/2\gamma$ for arbitrary L , thus proving the area-law entanglement scaling in the $\gamma \rightarrow 0$ limit.

In the SM [66], we explicitly calculate the trajectory-averaged entanglement entropy (as well as the classical entropy) for the monitored dynamics. We observe that in the periodic boundary conditions, the entanglement entropy scaling indeed undergoes a logarithm-to-area-law transition, while this transition is missing in the open boundary conditions. Also, in order to show the effect of the trajectory variance, as well as find a tighter bound on the entanglement entropy, we calculate the $\overline{S_{\text{cl}}[\{\langle n_i \rangle\}]}$.

In the above analysis, we consider only the $\theta = \pi$ case in the feedback operator, while similar FISE appears for arbitrary θ . In the SM [66], we show the numerical results for $\theta \neq \pi$. The length of the domain wall, however, is minimized at $\theta = \pi$. When θ approaches zero, we expect that the FISE still appears, although with a large domain wall that may exceed the numerical simulation capability. Therefore, for the projector P_i , the FISE is not a fine-

tuned phenomenon, and may appear for a large class of feedback operations.

Interacting system.— We demonstrate that the phenomenon of FISE persists in the interacting system, focusing on a spin-1/2 Hamiltonian

$$H = \sum_i [J_1(\sigma_i^x \sigma_{i+1}^x + \sigma_i^y \sigma_{i+1}^y) + J_z \sigma_i^z \sigma_{i+1}^z + J_2(\sigma_i^x \sigma_{i+2}^x + \sigma_i^y \sigma_{i+2}^y)]. \quad (14)$$

In Ref. [72], the non-integrable system (14) under continuous monitoring (on local σ_i^z) was shown to display a volume-to-area-law entanglement transition.

In our case, however, we choose the same generalized monitoring as in the free fermion case (via Jordan-Wigner transformation):

$$P_i = \frac{1}{2}(\sigma_i^+ - i\sigma_{i+1}^+)(\sigma_i^- + i\sigma_{i+1}^-), \quad U_i = S_{i+1}^z. \quad (15)$$

In the SM [66], we show that the generalized monitoring systems show a similar entanglement transition under periodic boundary conditions but display FISE under open boundary conditions. In the presence of FISE, the dynamics are primarily driven by the formation and fluctuation of domain walls. The area-law entanglement entropy due to FISE enables us to efficiently represent the states using matrix-product states [73, 74] and simulate time evolution for large system sizes using the TEBD algorithm [75, 76].

We investigate the steady-state classical entropy for different γ values and system sizes up to $L = 64$, and fix $J_1 = 0.5$, $J_z = 1.0$, $J_2 = 0.1$. As shown in Fig. 1f, the numerics indicate that for $\gamma > 0.5$, the classical entropy exhibits the asymptotic behavior:

$$S_{\text{cl}}(\gamma, t > t_{\text{rlx}}, L > L_{\text{DW}}) \approx \frac{1.8}{\gamma^{0.85}} \quad (16)$$

This suggests that a matrix product state with bond dimension $\chi \sim O(\exp(\gamma^{-0.85}))$ is sufficient to describe the state. However, the numerical simulation becomes challenging in the small γ regime. While we are unable to numerically verify the scaling behavior in the small γ limit due to computational limitations, our finite-size simulations still demonstrate the scaling law described by (as depicted in Fig. 1d)

$$S_{\text{cl}}(\gamma, t > t_{\text{rlx}}) = Lh(\gamma L^\nu), \quad (17)$$

where $\nu = 1.17$. We thus conjecture that the asymptotic form in Eq. (11) continues to hold in the small- γ regime.

Conclusion and discussion.— This work investigates the effect of generalized monitoring on the entanglement phase transition, with a particular focus on the emergence of the skin effect in certain open boundary monitored systems. Our analysis reveals that the skin effect qualitatively alters the entanglement structure of the nonequilibrium steady state, leading to a single area-law phase. Specifically, we show that introducing generic

feedback operators can disturb the balance of particle distribution, resulting in particle accumulation. We demonstrate that the FISE is not a fine-tuned phenomenon, as the skin effect appears for different feedback parameters, and survives in the presence of interactions. The suppression of the entanglement entropy from the skin effect also enables a sufficient classical simulation of the monitored interacted systems.

Readers may wonder whether FISE comes from the peculiar form of the projectors $\{P_i\}$, which do not commute with each other and is hard to realize experimentally. In the SM [66], we present a closely related monitored system where the monitored observable is the onsite particle occupation. Another interesting question is whether a generalized measurement (i.e., projective measurement followed by feedback) can lead to FISE. In the SM [66], we answer this question assertively, by proposing a simple model whose dynamics consist of a Floquet circuit evolution interspersed by generalized measurements.

These results have practical implications in the context of open systems or controllable quantum devices, as the monitoring-feedback setup can enable the realization of a skin effect without the need for post-selection in non-Hermitian dynamics. For systems showing FISE,

the steady states can be reached in constant steps, which is accessible for the noisy intermediate-scale quantum devices. In Fig. 2, we proposed a quantum circuit model displaying FISE (see SM [66] for detail), which can be experimentally realized on the trapped ions systems.

Note added.— In the middle of this work, we became aware of a recent work [77], which also considers the effect of generalized monitoring in the context of MIPT. The two works are complementary to each other: in Ref. [77], the authors utilize the feedback (pre-selection) to reveal MIPT as a quantum absorbing state transition that can be directly detected, while our work shows that the presence of conditional feedback may also eliminate the MIPT.

ACKNOWLEDGMENTS

J.R. thanks Chenguang Liang for the valuable discussions. J.R. and Y.P.W. thank Xu Feng and Shuo Liu for alerting them of a typo in the previous version. The numerical simulations based on tensor-network use the `ITensor` package [78].

-
- [1] Y. Li, X. Chen, and M. P. A. Fisher, Quantum zeno effect and the many-body entanglement transition, *Phys. Rev. B* **98**, 205136 (2018).
 - [2] B. Skinner, J. Ruhman, and A. Nahum, Measurement-induced phase transitions in the dynamics of entanglement, *Phys. Rev. X* **9**, 031009 (2019).
 - [3] A. Chan, R. M. Nandkishore, M. Pretko, and G. Smith, Unitary-projective entanglement dynamics, *Phys. Rev. B* **99**, 224307 (2019).
 - [4] Y. Li, X. Chen, and M. P. A. Fisher, Measurement-driven entanglement transition in hybrid quantum circuits, *Phys. Rev. B* **100**, 134306 (2019).
 - [5] L. Fidkowski, J. Haah, and M. B. Hastings, How Dynamical Quantum Memories Forget, *Quantum* **5**, 382 (2021).
 - [6] A. Nahum, S. Roy, B. Skinner, and J. Ruhman, Measurement and entanglement phase transitions in all-to-all quantum circuits, on quantum trees, and in Landau-ginsburg theory, *PRX Quantum* **2**, 010352 (2021).
 - [7] M. Ippoliti, M. J. Gullans, S. Gopalakrishnan, D. A. Huse, and V. Khemani, Entanglement phase transitions in measurement-only dynamics, *Phys. Rev. X* **11**, 011030 (2021).
 - [8] M. P. A. Fisher, V. Khemani, A. Nahum, and S. Vijay, Random quantum circuits (2022), [arXiv:2207.14280](https://arxiv.org/abs/2207.14280) [quant-ph].
 - [9] Y. Li, X. Chen, A. W. W. Ludwig, and M. P. A. Fisher, Conformal invariance and quantum nonlocality in critical hybrid circuits, *Phys. Rev. B* **104**, 104305 (2021).
 - [10] X. Chen, Y. Li, M. P. A. Fisher, and A. Lucas, Emergent conformal symmetry in nonunitary random dynamics of free fermions, *Phys. Rev. Research* **2**, 033017 (2020).
 - [11] A. Zabalo, M. J. Gullans, J. H. Wilson, S. Gopalakrishnan, D. A. Huse, and J. H. Pixley, Critical properties of the measurement-induced transition in random quantum circuits, *Phys. Rev. B* **101**, 060301(R) (2020).
 - [12] A. Chan, A. De Luca, and J. T. Chalker, Solution of a minimal model for many-body quantum chaos, *Phys. Rev. X* **8**, 041019 (2018).
 - [13] A. Nahum, S. Vijay, and J. Haah, Operator spreading in random unitary circuits, *Phys. Rev. X* **8**, 021014 (2018).
 - [14] C. W. von Keyserlingk, T. Rakovszky, F. Pollmann, and S. L. Sondhi, Operator hydrodynamics, otocs, and entanglement growth in systems without conservation laws, *Phys. Rev. X* **8**, 021013 (2018).
 - [15] T. Zhou and A. Nahum, Emergent statistical mechanics of entanglement in random unitary circuits, *Phys. Rev. B* **99**, 174205 (2019).
 - [16] M. P. A. Fisher, V. Khemani, A. Nahum, and S. Vijay, Random quantum circuits (2022), [arXiv:2207.14280](https://arxiv.org/abs/2207.14280) [quant-ph].
 - [17] O. Alberton, M. Buchhold, and S. Diehl, Entanglement transition in a monitored free-fermion chain: From extended criticality to area law, *Phys. Rev. Lett.* **126**, 170602 (2021).
 - [18] X. Cao, A. Tilloy, and A. D. Luca, Entanglement in a fermion chain under continuous monitoring, *SciPost Phys.* **7**, 024 (2019).
 - [19] M. Coppola, E. Tirrito, D. Karevski, and M. Collura, Growth of entanglement entropy under local projective measurements, *Phys. Rev. B* **105**, 094303 (2022).
 - [20] F. Carollo and V. Alba, Entangled multiplets and spreading of quantum correlations in a continuously monitored tight-binding chain, *Phys. Rev. B* **106**, L220304 (2022).
 - [21] X. Turkeshi, A. Biella, R. Fazio, M. Dalmonte, and M. Schiró, Measurement-induced entanglement transitions in the quantum Ising chain: From infinite to zero

- clicks, *Phys. Rev. B* **103**, 224210 (2021).
- [22] A. Biella and M. Schiró, Many-Body Quantum Zeno Effect and Measurement-Induced Subradiance Transition, *Quantum* **5**, 528 (2021).
- [23] T. Müller, S. Diehl, and M. Buchhold, Measurement-induced dark state phase transitions in long-ranged fermion systems, *Phys. Rev. Lett.* **128**, 010605 (2022).
- [24] T. Minato, K. Sugimoto, T. Kuwahara, and K. Saito, Fate of measurement-induced phase transition in long-range interactions, *Phys. Rev. Lett.* **128**, 010603 (2022).
- [25] M. Buchhold, Y. Minoguchi, A. Altland, and S. Diehl, Effective theory for the measurement-induced phase transition of dirac fermions, *Phys. Rev. X* **11**, 041004 (2021).
- [26] B. Ladewig, S. Diehl, and M. Buchhold, Monitored open fermion dynamics: Exploring the interplay of measurement, decoherence, and free hamiltonian evolution, *Phys. Rev. Research* **4**, 033001 (2022).
- [27] X. Turkeshi, L. Piroli, and M. Schiró, Enhanced entanglement negativity in boundary-driven monitored fermionic chains, *Phys. Rev. B* **106**, 024304 (2022).
- [28] A. Lavasani, Y. Alavirad, and M. Barkeshli, Measurement-induced topological entanglement transitions in symmetric random quantum circuits, *Nature Physics* **17**, 342 (2021).
- [29] M. Ippoliti, M. J. Gullans, S. Gopalakrishnan, D. A. Huse, and V. Khemani, Entanglement phase transitions in measurement-only dynamics, *Phys. Rev. X* **11**, 011030 (2021).
- [30] R. Vasseur, A. C. Potter, Y.-Z. You, and A. W. W. Ludwig, Entanglement transitions from holographic random tensor networks, *Phys. Rev. B* **100**, 134203 (2019).
- [31] J. Lopez-Piqueres, B. Ware, and R. Vasseur, Mean-field entanglement transitions in random tree tensor networks, *Phys. Rev. B* **102**, 064202 (2020).
- [32] C.-M. Jian, B. Bauer, A. Keselman, and A. W. W. Ludwig, Criticality and entanglement in non-unitary quantum circuits and tensor networks of non-interacting fermions (2022), [arXiv:2012.04666 \[cond-mat.stat-mech\]](https://arxiv.org/abs/2012.04666).
- [33] Z.-C. Yang, Y. Li, M. P. A. Fisher, and X. Chen, Entanglement phase transitions in random stabilizer tensor networks, *Phys. Rev. B* **105**, 104306 (2022).
- [34] S. Choi, Y. Bao, X.-L. Qi, and E. Altman, Quantum error correction in scrambling dynamics and measurement-induced phase transition, *Phys. Rev. Lett.* **125**, 030505 (2020).
- [35] M. J. Gullans and D. A. Huse, Scalable probes of measurement-induced criticality, *Phys. Rev. Lett.* **125**, 070606 (2020).
- [36] M. J. Gullans and D. A. Huse, Dynamical purification phase transition induced by quantum measurements, *Phys. Rev. X* **10**, 041020 (2020).
- [37] M. J. Gullans, S. Krastanov, D. A. Huse, L. Jiang, and S. T. Flammia, Quantum coding with low-depth random circuits, *Phys. Rev. X* **11**, 031066 (2021).
- [38] A. J. Daley, Quantum trajectories and open many-body quantum systems, *Advances in Physics* **63**, 77 (2014), <https://doi.org/10.1080/00018732.2014.933502>.
- [39] Y. Bao, S. Choi, and E. Altman, Theory of the phase transition in random unitary circuits with measurements, *Phys. Rev. B* **101**, 104301 (2020).
- [40] C.-M. Jian, Y.-Z. You, R. Vasseur, and A. W. W. Ludwig, Measurement-induced criticality in random quantum circuits, *Phys. Rev. B* **101**, 104302 (2020).
- [41] Y. Li and M. P. A. Fisher, Statistical mechanics of quantum error correcting codes, *Phys. Rev. B* **103**, 104306 (2021).
- [42] Y. Li, R. Vasseur, M. P. A. Fisher, and A. W. W. Ludwig, Statistical mechanics model for clifford random tensor networks and monitored quantum circuits (2021).
- [43] X. Turkeshi, M. Dalmonte, R. Fazio, and M. Schiró, Entanglement transitions from stochastic resetting of non-hermitian quasiparticles, *Phys. Rev. B* **105**, L241114 (2022).
- [44] M. Ippoliti and V. Khemani, Postselection-free entanglement dynamics via spacetime duality, *Phys. Rev. Lett.* **126**, 060501 (2021).
- [45] M. Ippoliti, T. Rakovszky, and V. Khemani, Fractal, logarithmic, and volume-law entangled nonthermal steady states via spacetime duality, *Phys. Rev. X* **12**, 011045 (2022).
- [46] T. Iadecola, S. Ganeshan, J. H. Pixley, and J. H. Wilson, Dynamical entanglement transition in the probabilistic control of chaos (2022), [arXiv:2207.12415 \[cond-mat.dis-nn\]](https://arxiv.org/abs/2207.12415).
- [47] G. Kells, D. Meidan, and A. Romito, Topological transitions in weakly monitored free fermions, *SciPost Phys.* **14**, 031 (2023).
- [48] X. Turkeshi and M. Schiró, Entanglement and correlation spreading in non-hermitian spin chains, *Phys. Rev. B* **107**, L020403 (2023).
- [49] S.-K. Jian, Z.-C. Yang, Z. Bi, and X. Chen, Yang-lee edge singularity triggered entanglement transition, *Phys. Rev. B* **104**, L161107 (2021).
- [50] K. Kawabata, T. Numasawa, and S. Ryu, Entanglement phase transition induced by the non-hermitian skin effect (2022), [arXiv:2206.05384 \[cond-mat.stat-mech\]](https://arxiv.org/abs/2206.05384).
- [51] S. Gopalakrishnan and M. J. Gullans, Entanglement and purification transitions in non-hermitian quantum mechanics, *Phys. Rev. Lett.* **126**, 170503 (2021).
- [52] S. Yao and Z. Wang, Edge states and topological invariants of non-hermitian systems, *Phys. Rev. Lett.* **121**, 086803 (2018).
- [53] V. M. Martinez Alvarez, J. E. Barrios Vargas, and L. E. F. Foa Torres, Non-hermitian robust edge states in one dimension: Anomalous localization and eigenspace condensation at exceptional points, *Phys. Rev. B* **97**, 121401(R) (2018).
- [54] K. Zhang, Z. Yang, and C. Fang, Correspondence between winding numbers and skin modes in non-hermitian systems, *Phys. Rev. Lett.* **125**, 126402 (2020).
- [55] K. Yokomizo and S. Murakami, Non-bloch band theory of non-hermitian systems, *Phys. Rev. Lett.* **123**, 066404 (2019).
- [56] N. Okuma, K. Kawabata, K. Shiozaki, and M. Sato, Topological origin of non-hermitian skin effects, *Phys. Rev. Lett.* **124**, 086801 (2020).
- [57] Z. Yang, K. Zhang, C. Fang, and J. Hu, Non-hermitian bulk-boundary correspondence and auxiliary generalized brillouin zone theory, *Phys. Rev. Lett.* **125**, 226402 (2020).
- [58] D. S. Borgnia, A. J. Kruchkov, and R.-J. Slager, Non-hermitian boundary modes and topology, *Phys. Rev. Lett.* **124**, 056802 (2020).
- [59] L. E. F. F. Torres, Perspective on topological states of non-hermitian lattices, *Journal of Physics: Materials* **3**, 014002 (2019).
- [60] K. Jacobs and D. A. Steck, A straightforward introduction to continuous quantum measure-

- ment, *Contemporary Physics* **47**, 279 (2006), <https://doi.org/10.1080/00107510601101934>.
- [61] H. M. Wiseman and G. J. Milburn, *Quantum Measurement and Control* (Cambridge University Press, 2009).
- [62] A. Barchielli and M. Gregoratti, The stochastic schrödinger equation, in *Quantum Trajectories and Measurements in Continuous Time: The Diffusive Case* (Springer Berlin Heidelberg, Berlin, Heidelberg, 2009) pp. 11–49.
- [63] G. Lindblad, On the generators of quantum dynamical semigroups, *Communications in Mathematical Physics* **48**, 119 (1976).
- [64] E. B. Davies, Markovian master equations, *Communications in Mathematical Physics* **39**, 91 (1974).
- [65] H.-P. Breuer and F. Petruccione, *The Theory of Open Quantum Systems* (Oxford University Press, 2007).
- [66] See Supplemental Material for detail regarding the stochastic Schrödinger Equation, the uniqueness of nonequilibrium steady state, the numerical simulations of projective monitoring dynamics, the trajectory averaging of classical entropy of generalized monitoring, the numerical simulations of interacted monitoring dynamics, the monitored free fermion with different conditional feedback, the additional generalized monitored model, the measured Floquet circuit model displaying skin effect, and the experimental proposal on the trapped ions quantum computers, which also includes Refs. [79–86].
- [67] M. A. Nielsen and I. L. Chuang, *Quantum Computation and Quantum Information: 10th Anniversary Edition* (Cambridge University Press, 2010).
- [68] M. M. Wilde, *Quantum Information Theory* (Cambridge University Press, 2013).
- [69] N. Hatano and D. R. Nelson, Localization transitions in non-hermitian quantum mechanics, *Phys. Rev. Lett.* **77**, 570 (1996).
- [70] In contrast, when γ is sufficiently large ($\gamma \sim O(c)$), the lattice effect becomes prominent, and the scaling behavior breaks down.
- [71] R. A. Horn and C. R. Johnson, *Topics in Matrix Analysis* (Cambridge University Press, 1991).
- [72] Y. Fuji and Y. Ashida, Measurement-induced quantum criticality under continuous monitoring, *Phys. Rev. B* **102**, 054302 (2020).
- [73] M. Fannes, B. Nachtergaele, and R. F. Werner, Finitely correlated states on quantum spin chains, *Communications in Mathematical Physics* **144**, 443 (1992).
- [74] M. W. J. C. D. Perez-Garcia, F. Verstraete, Matrix product state representations (2007), [arXiv:quant-ph/0608197](https://arxiv.org/abs/quant-ph/0608197).
- [75] G. Vidal, Efficient classical simulation of slightly entangled quantum computations, *Phys. Rev. Lett.* **91**, 147902 (2003).
- [76] G. Vidal, Classical simulation of infinite-size quantum lattice systems in one spatial dimension, *Phys. Rev. Lett.* **98**, 070201 (2007).
- [77] M. Buchhold, T. Müller, and S. Diehl, Revealing measurement-induced phase transitions by pre-selection (2022), [arXiv:2208.10506](https://arxiv.org/abs/2208.10506) [cond-mat.dis-nn].
- [78] M. Fishman, S. R. White, and E. M. Stoudenmire, The ITensor software library for tensor network calculations (2020), [arXiv:2007.14822](https://arxiv.org/abs/2007.14822).
- [79] W. Berdanier, J. Marino, and E. Altman, Universal dynamics of stochastically driven quantum impurities, *Phys. Rev. Lett.* **123**, 230604 (2019).
- [80] S. Bravyi, Lagrangian representation for fermionic linear optics [10.48550/ARXIV.QUANT-PH/0404180](https://arxiv.org/abs/10.48550/ARXIV.QUANT-PH/0404180) (2004).
- [81] W. Paul, Electromagnetic traps for charged and neutral particles, *Rev. Mod. Phys.* **62**, 531 (1990).
- [82] J. I. Cirac and P. Zoller, Quantum computations with cold trapped ions, *Phys. Rev. Lett.* **74**, 4091 (1995).
- [83] D. Hayes, D. N. Matsukevich, P. Maunz, D. Hucul, Q. Quraishi, S. Olmschenk, W. Campbell, J. Mizrahi, C. Senko, and C. Monroe, Entanglement of atomic qubits using an optical frequency comb, *Phys. Rev. Lett.* **104**, 140501 (2010).
- [84] K. Mølmer and A. Sørensen, Multiparticle entanglement of hot trapped ions, *Phys. Rev. Lett.* **82**, 1835 (1999).
- [85] D. Porras and J. I. Cirac, Effective quantum spin systems with trapped ions, *Phys. Rev. Lett.* **92**, 207901 (2004).
- [86] S.-L. Zhu, C. Monroe, and L.-M. Duan, Arbitrary-speed quantum gates within large ion crystals through minimum control of laser beams, *Europhysics Letters* **73**, 485 (2006).
- [87] D. E. Evans, Irreducible quantum dynamical semigroups, *Communications in Mathematical Physics* **54**, 293 (1977).
- [88] A. Frigerio, Stationary states of quantum dynamical semigroups, *Communications in Mathematical Physics* **63**, 269 (1978).
- [89] H. Spohn, Kinetic equations from hamiltonian dynamics: Markovian limits, *Rev. Mod. Phys.* **52**, 569 (1980).
- [90] T. Prosen, Matrix product solutions of boundary driven quantum chains, *Journal of Physics A: Mathematical and Theoretical* **48**, 373001 (2015).
- [91] Y. Fuji and Y. Ashida, Measurement-induced quantum criticality under continuous monitoring, *Phys. Rev. B* **102**, 054302 (2020).

Supplemental Materials for “Absence of entanglement transition due to feedback-induced skin effect”

CONTENTS

Acknowledgments	5
References	5
1. Stochastic Schrödinger equation	S1
1.1. Generalized monitoring	S1
1.2. Free fermion simulation	S3
2. Uniqueness of nonequilibrium steady state	S5
2.1. Projective monitoring	S5
2.2. Generalized monitoring and interactions	S6
3. Numerical simulations of projective monitoring dynamics	S6
4. Trajectory averaging of classical entropy of generalized monitoring	S8
5. Numerical simulations of interacted monitoring dynamics	S10
6. Monitored free fermion with different conditional feedback	S10
7. Additional generalized monitored model	S12
8. Measured Floquet circuit model displaying skin effect	S14
8.1. Wave packet motion under Floquet evolution	S14
8.2. Measurement dynamics	S15
9. Experimental proposal on the trapped ions quantum computers	S16

Appendix 1: Stochastic Schrödinger equation

1.1. Generalized monitoring

Microscopically, a measurement process involves a short-time interaction between the system and the probe, which are initially separable:

$$|\psi_{AB}\rangle = e^{-iH_{\text{int}}\Delta t}|\psi_A\rangle \otimes |\psi_B\rangle, \quad (\text{S1})$$

where the wave function of the measured system is denoted as $|\psi_A\rangle$ and the probe $|\psi_B\rangle$. When Δt is much smaller than the time scale of the system, the system can be regarded as static during the measurement. Such measurement is called the *strong measurement*. The probe is thought to be a device that can convert quantum information to the classical one, which takes the form of standard projective measurement. That is, suppose the eigenbasis of the probe is $\{|\phi_n\rangle\}$, the probability of getting a record n is

$$p_n = \langle \phi_n | \rho_B | \phi_n \rangle, \quad \rho_B \equiv \text{Tr}_A |\psi_{AB}\rangle \langle \psi_{AB}|, \quad (\text{S2})$$

and the feedback of the measurement to the system is

$$|\tilde{\psi}_A^{(n)}\rangle = \langle \phi_n | e^{-iH_{\text{int}}\Delta t} |\psi_A\rangle \otimes |\psi_B\rangle \equiv M_n |\psi_A\rangle. \quad (\text{S3})$$

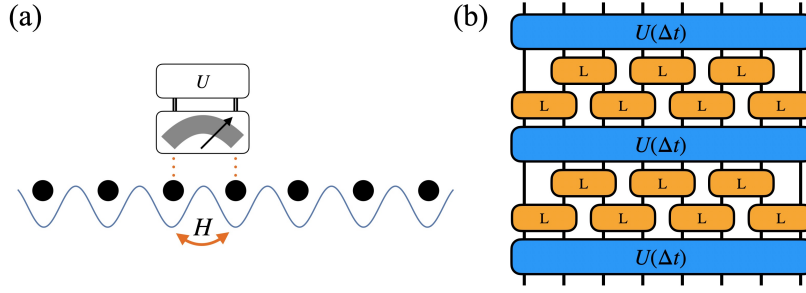


FIG. S1. (a) Schematic of a fermion chain under nearest neighbor interaction and generalized monitoring on each pair of neighboring sites. Unitary feedback will be applied if the probe records a quantum jump. (b) Circuits representation of the discretized Hamiltonian evolution with constant monitoring.

The completeness condition requires

$$\sum_n \langle \tilde{\psi}_A^{(n)} | \tilde{\psi}_A^{(n)} \rangle = 1 \implies \sum_n M_n^\dagger M_n = 1. \quad (\text{S4})$$

This is the general form of the measure. In the language of density operator, a measurement is described by a set of operators $\{M_n\}$. A measurement process may record a result n with probability p_n and change the state to:

$$\rho \rightarrow \frac{M_n \rho M_n^\dagger}{\|M_n \rho M_n^\dagger\|}. \quad (\text{S5})$$

If the measurement result is not known, the averaged density matrix after the measurement is

$$\rho \rightarrow \sum_n M_n \rho M_n^\dagger. \quad (\text{S6})$$

Such a map is called the quantum channel [67].

On the other hand, if the strength of system-probe coupling is comparable with the energy scale of the system, which is the case for an open quantum system, the quantum channel expression should depend on time Δt . This kind of measurement process is called *weak measurement*. When the system is *Markovian* (the equation of motion depends only on the near past), the course-grained dissipation process can be described by the channel:

$$\begin{aligned} M_n &= L_n \sqrt{\gamma \Delta t}, \\ M_0 &= \sqrt{1 - \sum_{n>0} M_n^\dagger M_n} = 1 - \frac{\gamma}{2} \sum_{n>0} L_n^\dagger L_n \Delta t + O(\Delta t^2). \end{aligned} \quad (\text{S7})$$

For the density matrix, the coarse-grained differential equation is the Lindblad equation:

$$\begin{aligned} \frac{d\rho}{dt} &= \lim_{\Delta t \rightarrow 0} \frac{1}{\Delta t} \sum_n M_n e^{-iH\Delta t} \rho e^{iH\Delta t} M_n^\dagger \\ &= -i[H, \rho] - \frac{\gamma}{2} \sum_i \{L_i^\dagger L_i, \rho\} + \gamma \sum_i L_i \rho L_i^\dagger. \end{aligned} \quad (\text{S8})$$

The joint dynamics of Hamiltonian evolution and measurement can be equivalently described by the stochastic process, as shown in Fig. S1, where for each time step Δt , the system first undergoes a coherent evolution $|\psi\rangle \rightarrow e^{-iH\Delta t}|\psi\rangle$, then the application of measurement produces a random process:

$$|\psi\rangle \rightarrow \begin{cases} M_n(\Delta t)|\psi\rangle & P_n = \langle \psi | L_n^\dagger L_n | \psi \rangle \gamma \Delta t \\ M_0(\Delta t)|\psi\rangle & P_0 = 1 - \sum_{n>0} P_n \end{cases}. \quad (\text{S9})$$

Different records of the measurement result correspond to different trajectories, and the Lindblad equation is equivalent to the trajectory averaged of such stochastic processes. In the continuum limit, the stochastic differential equation

can be formulated by introducing a Poisson random variable dW_n taking the discrete values of 0 or 1. The $dW_n = 1$ case corresponds to registering a quantum jump, otherwise, $dW_n = 0$. The expectation value for random dW_n is proportional to dt :

$$\overline{dW}_n = \langle \psi | L_n^\dagger L_n | \psi \rangle \gamma dt. \quad (\text{S10})$$

Different dW_n 's are independent, i.e., they satisfy the orthogonal condition

$$dW_m dW_n = \delta_{mn} dW_m. \quad (\text{S11})$$

Therefore, the random quantum jump process $|\psi\rangle \rightarrow M_n|\psi\rangle$ is described by the expression

$$d|\psi\rangle = \left(\frac{L_n}{\sqrt{\langle L_n^\dagger L_n \rangle}} - 1 \right) |\psi\rangle dW_n, \quad (\text{S12})$$

and the null-detection case correspond to $|\psi\rangle \rightarrow M_0|\psi\rangle$, which is described by a non-Hermitian differential equation:

$$d|\psi\rangle = -\frac{\gamma}{2} \sum_m (L_m^\dagger L_m - \langle L_m^\dagger L_m \rangle) |\psi\rangle dt, \quad (\text{S13})$$

where the $\langle L_m^\dagger L_m \rangle$ is introduced for the normalization purpose. Together with the coherent evolution, we obtain the stochastic Schrödinger equation in the main text:

$$d|\psi\rangle = \left[-iH - \frac{\gamma}{2} \sum_m (L_m^\dagger L_m - \langle L_m^\dagger L_m \rangle) \right] |\psi\rangle dt + \sum_m \left(\frac{L_m}{\sqrt{\langle L_m^\dagger L_m \rangle}} - 1 \right) |\psi\rangle dW_m. \quad (\text{S14})$$

1.2. Free fermion simulation

For numerical simulation of Eq. (S14), we can first discretize the time into small interval Δt . The discrete evolution is then

$$|\psi(t + \Delta t)\rangle = \mathcal{M}_{\Delta t} [e^{-iH_{\text{eff}}\Delta t} |\psi(t)\rangle], \quad (\text{S15})$$

where $\mathcal{M}_{\Delta t}$ represents the quantum jump that randomly happened in time interval Δt :

$$\mathcal{M}_{\Delta t} [|\psi\rangle] \propto \prod_{m \in I} L_m |\psi\rangle. \quad (\text{S16})$$

In the Eq. (S16), the set I denotes the random jump processes, which can be obtained by

$$I = \{n | r_n < \gamma \langle L_n^\dagger L_n \rangle \Delta t\}, \quad (\text{S17})$$

where $\{r_n \in (0, 1)\}$ is a set of independent random variables with evenly distributed probability.

The free fermion system can be efficiently represented by the Gaussian state [80]. For a particle number conserving system, the Gaussian state is a quasimode-occupied state, represented by a matrix B :

$$|B\rangle \equiv \prod_{j=1}^N \sum_i B_{ij} c_i^\dagger |0\rangle = \bigotimes_{j=1}^N |B_j\rangle, \quad (\text{S18})$$

where each column B_j is an occupied quasimode. Note that there is an $SU(N)$ gauge freedom for the matrix B , i.e.,

$$|B'\rangle = |BU\rangle = |B\rangle, \quad (\text{S19})$$

where U is an arbitrary $SU(N)$ matrix. Such gauge freedom implies that a Gaussian state is entirely specified by the linear subspace spanned by the quasimodes B_i 's.

The random Schrödinger equation can be Trotterized as Eq. (S15). Using the Baker-Campbell-Hausdor formula $e^A B e^{-A} = e^{\text{ad}_A} B$, the nonunitary evolution is

$$\begin{aligned}
e^{-iH_{\text{eff}}\Delta t}|B_t\rangle &= \prod_{j=1}^N \sum_i B_{ij} e^{-iH_{\text{eff}}\Delta t} c_i^\dagger e^{iH_{\text{eff}}\Delta t} |0\rangle \\
&= \prod_{j=1}^N \sum_i B_{ij} e^{-i\Delta t[H_{\text{eff}}, \cdot]} c_i^\dagger |0\rangle \\
&= \prod_{j=1}^N \sum_i \sum_k B_{ij} c_k^\dagger [e^{-iH_{\text{eff}}\Delta t}]_{ki} |0\rangle \\
&= \prod_{j=1}^N \sum_k [e^{-iH_{\text{eff}}\Delta t} B_{ij}]_{kj} c_k^\dagger |0\rangle \\
&= |e^{-iH_{\text{eff}}\Delta t} B_t\rangle.
\end{aligned} \tag{S20}$$

That is, the matrix is multiplied by the exponential of the effective non-Hermitian (single-body) Hamiltonian matrix. Note that the resulting matrix is not orthogonal anymore, while the state is still well-defined by the linear space spanned by those unorthogonal vectors. In general, for a Gaussian state represented by matrix B , we can obtain a canonical form for the representing matrix using the QR decomposition $B = Q \cdot R$, where Q is a unitary matrix and R is upper triangular. Note that Q and B span the same linear space, so the Gaussian state can be expressed as $|Q\rangle$.

The supper operator $\mathcal{M}_{\Delta t}$ in Eq. (S15) corresponds to the Poisson jump process, where for each index i , we randomly decide whether a quantum jump process

$$|B\rangle \rightarrow \frac{L_i|B\rangle}{\|L_i|B\rangle\|} \tag{S21}$$

happens, with the probability

$$p_i = \langle B|L_i^\dagger L_i|B\rangle \gamma \Delta t \tag{S22}$$

The L_m 's we choose in the main text have the form

$$L_m = e^{ih} d^\dagger d, \quad d^\dagger = \sum_i a_i c_i^\dagger, \quad h = \sum_{ij} h_{ij} c_i^\dagger c_j, \tag{S23}$$

where d^\dagger is a quasimode, and h is a fermion bilinear. The following shows that the Gaussian form is preserved by such jump operator L_m . First, the probability of the jump process is

$$\langle B|L_m^\dagger L_m|B\rangle = \langle B|d^\dagger d|B\rangle = \|d|B\rangle\|^2. \tag{S24}$$

The action of annihilation operator d on $|B\rangle$ is

$$d|B\rangle = \sum_k a_k^* c_k \prod_j \sum_i c_i^\dagger B_{ij} |0\rangle = \sum_j \langle a|B_j\rangle \bigotimes_{l \neq j} |B_l\rangle, \tag{S25}$$

so we can obtain the probability

$$p_m = \sum_j |\langle a|B_j\rangle|^2 \gamma \Delta t. \tag{S26}$$

Besides, we can utilize the gauge freedom to choose the basis such that $\langle a|B'_j\rangle = 0$ for $j > 1$. The matrix B' always exists since we can always find a column j that $\langle a|B_j\rangle \neq 0$ (otherwise, the probability of the jump is zero). We then move the column to the first and define the column as

$$|B'_j\rangle = |B_j\rangle - \frac{\langle a|B_j\rangle}{\langle a|B_1\rangle} |B_1\rangle, \quad j > 1. \tag{S27}$$

Note that such column transformation does not alter the linear space B spans, while the orthogonality and the normalization might be affected and should be renormalized afterward. Eq. (S25) then simplified to:

$$d|B\rangle = \bigotimes_{j>1} |B'_j\rangle. \tag{S28}$$

The result of the quantum jump is

$$L_m|B\rangle = |e^{ih}a\rangle \bigotimes_{j>1} |e^{ih}B'_j\rangle. \quad (\text{S29})$$

The representation of the outcome state is also not orthogonal. An additional QR decomposition is needed to convert it to canonical form.

Appendix 2: Uniqueness of nonequilibrium steady state

In this section, we prove the uniqueness of ρ_{NESS} for models considered in the main text. We first note that for the projective monitored dynamics, all jump operators $\{P_i\}$ are Hermitian. The maximally mixed state within a given particle-number sector $\rho = \mathbb{I}_\nu$ (the subscript indicates the subspace spanned by the states of filling number ν) is automatically a steady state:

$$\begin{aligned} \frac{d}{dt}\mathbb{I}_\nu &= -\frac{\gamma}{2} \sum_m \{P_m, \mathbb{I}_\nu\} + \gamma \sum_m P_m \mathbb{I}_\nu P_m^\dagger \\ &= -\gamma \sum_m P_m|_\nu + \gamma \sum_m P_m|_\nu \\ &= 0. \end{aligned} \quad (\text{S1})$$

In addition, ρ_{NESS} for generic Lindblad equation is nondegenerate [87–90]. That is, even if we encounter an accidental degeneracy of ρ_{NESS} , we can usually find a suitable boundary perturbation to break the degeneracy.

In Refs. [87, 88] (see review in Ref. [89] and application in Ref. [90], where the system is under boundary driven [79]), it was shown that a Lindblad equation has unique nonequilibrium steady state if and only if the set

$$\{H, L_1, L_1^\dagger, L_2, L_2^\dagger, \dots\} \quad (\text{S2})$$

generates (under multiplication and addition) the complete algebra on the Hilbert space. The general proof assumes no conserved quantity for the Lindblad equation. For the particle number conserving case, as we considered in the main text, we can focus on the Hilbert subspace \mathcal{H}_N spanned by N -particle states. The uniqueness condition then says if $\{H, L_1, L_1^\dagger, L_2, L_2^\dagger, \dots\}$ generates the complete algebra on \mathcal{H}_N , the steady state in \mathcal{H}_N will be unique.

2.1. Projective monitoring

We first prove that the Hamiltonian (under open boundary conditions)

$$H = \sum_i (c_i^\dagger c_{i+1} + c_{i+1}^\dagger c_i) \quad (\text{S3})$$

and the projectors

$$P_i = \frac{1}{2}(c_i^\dagger - ic_{i+1}^\dagger)(c_i + ic_{i+1}) \quad (\text{S4})$$

generate the whole algebra. Note H and P_1, P_2 together generate the following particle number operators:

$$\begin{aligned} n_1 - n_3 &= P_2 - P_1 + i[H, P_1 + P_2], \\ n_1 + n_2 &= \frac{1}{2}(P_1 + P_2 + i[H, n_1 - n_3] + n_1 - n_3), \\ n_2 + n_3 &= (n_1 + n_2) - (n_1 - n_3). \end{aligned} \quad (\text{S5})$$

Then, some straightforward algebra lead to

$$\begin{aligned} c_1^\dagger c_2 - c_2^\dagger c_1 &= i(n_1 + n_2) - iP_1, \\ c_1^\dagger c_2 + c_2^\dagger c_1 &= [c_1^\dagger c_2 - c_2^\dagger c_1, n_2 + n_3], \\ c_2^\dagger c_3 - c_3^\dagger c_2 &= i(n_2 + n_3) - iP_2, \\ c_2^\dagger c_3 + c_3^\dagger c_2 &= [n_1 + n_2, c_2^\dagger c_3 - c_3^\dagger c_2]. \end{aligned} \quad (\text{S6})$$

Upon some addition among Eqs. (S6), we obtain the operator $c_1^\dagger c_2$, $c_2^\dagger c_3$ and their Hermitian conjugates. The commutations of them further produce $c_1^\dagger c_3$ and its conjugate. Also, note that

$$[c_1^\dagger c_2, c_2^\dagger c_1] = n_1 - n_2. \quad (\text{S7})$$

Together with Eqs. (S5), we generate all fermion bilinear terms $c_i^\dagger c_j$ (including $i = j$ case) on sites $(1, 2, 3)$. To proceed, we subtract the hopping terms between sites $(1, 2)$ from H . The resulting operator is equivalent to a shorter chain starting from site 2. We can then utilize the calculation above to obtain all $c_i^\dagger c_j$ terms on sites $(2, 3, 4)$. We eventually obtain all fermion bilinear terms on the chain by applying the strategy iteratively. Note that fermion bilinear terms $c_i^\dagger c_j$ generate the complete algebra within a fixed particle-number sector since any two product states in the sector can be related by applying several fermion hopping terms.

2.2. Generalized monitoring and interactions

For the generalized monitored system described by the jump operators $\{L_n = U_n P_n\}$, the proof of uniqueness is essentially the same as the projective case. Note that we can generate all P_i terms by multiplying to jump operators

$$P_i = L_i^\dagger L_i. \quad (\text{S8})$$

In this way, we can generate the complete operator algebra in the same way as above.

We argue that the completeness of the operator algebra holds for generic open systems since the exact decoupling of Hilbert space is the result of symmetries or fine-tuning. For the interacting system where the Hamiltonian is

$$H = \sum_i (c_i^\dagger c_{i+1} + c_{i+1}^\dagger c_i + g n_i n_{i+1}). \quad (\text{S9})$$

The above argument means for a random value of g , we should expect the completeness of the operator algebra. We can also consider the case where the coupling constant is smoothly varying in the space. In particular, let $g_i = 0$ for the sites near the boundary. Following the same procedure, we can generate the operator algebra of the subsystem near the boundary. Assume that we meet the first nonzero g at site $i+1$. It means that we have the complete operator algebra (within fixed filling number) $\mathcal{A}_{[1,i]}$ of the subsystem consisting of sites $1, \dots, i$. We first subtract all terms within $\mathcal{A}_{[1,i]}$ from the Hamiltonian and denote the result as $H_{[i+1,N]}$. Consider the commutators

$$\begin{aligned} [n_{i-1}, H_{[i+1,N]}] &= c_i^\dagger c_{i+1} - c_{i+1}^\dagger c_i, \\ [n_{i-1}, c_i^\dagger c_{i+1} - c_{i+1}^\dagger c_i] &= c_i^\dagger c_{i+1} + c_{i+1}^\dagger c_i. \end{aligned} \quad (\text{S10})$$

In this way, we generate the hopping terms $c_i^\dagger c_{i+1}$ and $c_{i+1}^\dagger c_i$. Those terms together with $\mathcal{A}_{[1,i]}$ generate the algebra $\mathcal{A}_{[1,i+1]}$. This procedure can proceed iteratively, therefore producing the complete algebra.

Appendix 3: Numerical simulations of projective monitoring dynamics

We have demonstrated that a general Lindblad equation,

$$\frac{d}{dt}\rho = -i[H, \rho] + \gamma \sum_i L_i \rho L_i^\dagger - \frac{1}{2} \left\{ L_i^\dagger L_i, \rho \right\}, \quad \text{where } L_i \text{ are projectors,} \quad (\text{S1})$$

leads to a unique and homogeneous steady state (under open boundary conditions). In this section, we present numerical evidence supporting the homogeneity of late-time states for typical stochastic trajectories, described by:

$$d|\psi\rangle = \left[-iH - \frac{\gamma}{2} \sum_m (L_m^\dagger L_m - \langle L_m^\dagger L_m \rangle) \right] |\psi\rangle dt + \sum_m \left(\frac{L_m}{\sqrt{\langle L_m^\dagger L_m \rangle}} - 1 \right) |\psi\rangle dW_m. \quad (\text{S2})$$

That is, the spatial homogeneity is not only at the density matrix level but also at the trajectory level. This suggests that the skin effect, which suppresses entanglement entropy, does not arise within the projective monitoring system. Therefore, introducing conditional feedback is essential to induce a dynamical skin effect.

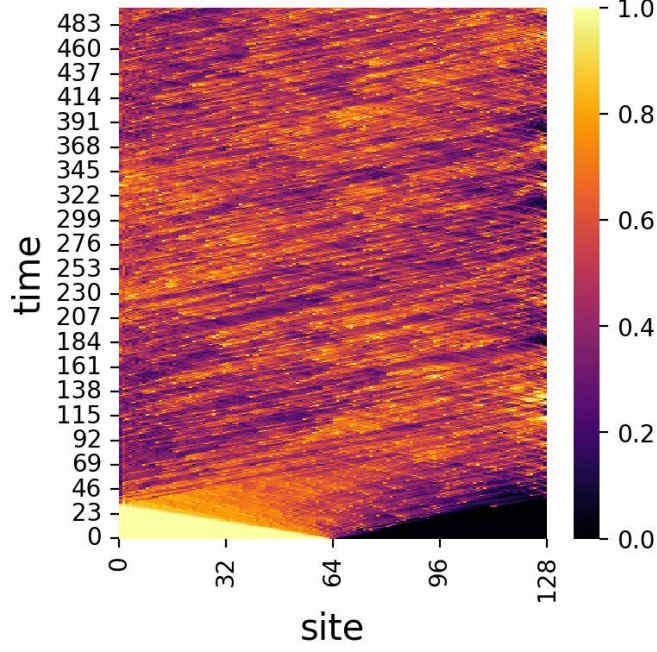


FIG. S2. A typical trajectory's density evolution of a projective monitored system with $\gamma = 0.1$, $L = 128$, under open boundary condition. Although monitoring creates random quantum jump processes and thus introduces density fluctuation, the density distribution on a large scale is homogeneous.

In the following, we consider the model studied in the main text, of which the unitary evolution is generated by the Hamiltonian:

$$H = \sum_i (c_i^\dagger c_{i+1} + c_{i+1}^\dagger c_i) \quad (\text{S3})$$

and the monitoring is described by

$$L_i = \frac{1}{2}(c_i^\dagger - ic_{i+1}^\dagger)(c_i + ic_{i+1}). \quad (\text{S4})$$

Fig. S2 depicts the evolution of particle density for a typical trajectory. At late times, the system reaches a homogeneous state with only minor fluctuations.

To further analyze the homogeneity of trajectories' densities, in Fig. S3a, we plot the trajectory-averaged classical entropy:

$$S_{\text{cl}} = -\overline{\sum_i [\langle n_i \rangle \log \langle n_i \rangle + (1 - \langle n_i \rangle) \log(1 - \langle n_i \rangle)]}. \quad (\text{S5})$$

We observe a linear growth with system size, indicating a highly homogeneous density distribution. Moreover, when γ is small, the growth of the classical entropy approaches the saturation value

$$S_{\text{max}} = L \log 2, \quad (\text{S6})$$

which means that most trajectory has nearly homogeneous density distribution.

In contrast, Fig. S3b shows the entanglement entropy, which is considerably smaller than the classical entropy and exhibits an entanglement transition from log law to area law. These results suggest that the projective monitoring system under open boundary conditions may undergo a measurement-induced entanglement phase transition, similar to the periodic boundary condition.

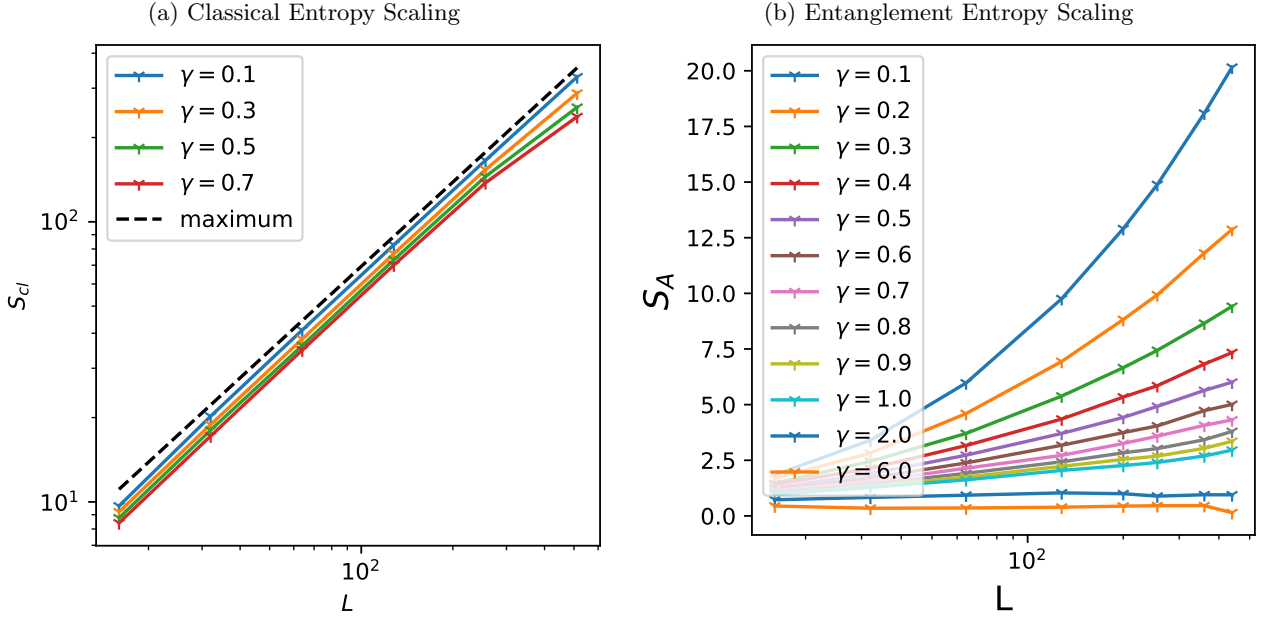


FIG. S3. (a) Scaling of trajectory-averaged classical entropies for $L = [16, 32, 634, 128, 256, 512]$. (b) Scaling of entanglement entropy for $L = [16, 32, 634, 128, 256, 512]$.

Appendix 4: Trajectory averaging of classical entropy of generalized monitoring

In this section, we revisit the monitoring system with feedback, of which the unitary evolution is generated by the Hamiltonian:

$$H = \sum_i (c_i^\dagger c_{i+1} + c_{i+1}^\dagger c_i) \quad (\text{S1})$$

and the monitoring is described by

$$L_i = \frac{1}{2} e^{-i\pi n_{i+1}} (c_i^\dagger - i c_{i+1}^\dagger) (c_i + i c_{i+1}). \quad (\text{S2})$$

Fig. S4a illustrates the trajectory averaging of entanglement entropy. The entanglement entropy exhibits a transition from log law to area law.

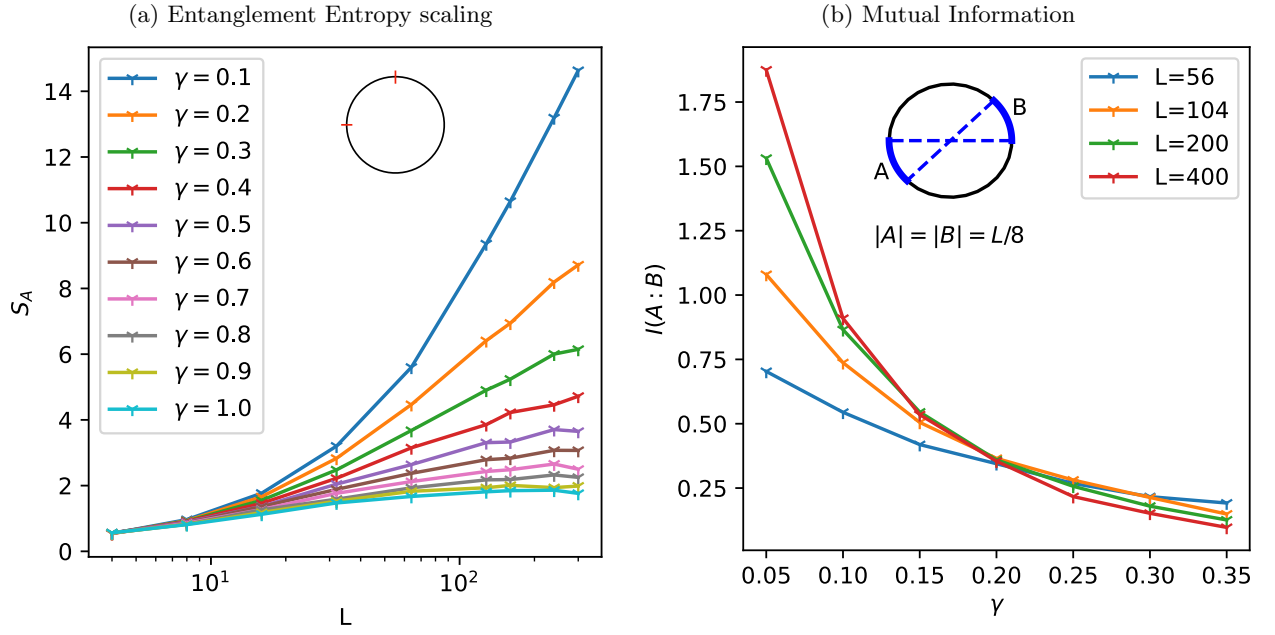


FIG. S4. (a) Trajectory average of entanglement entropy for different measurement rates. (b) Trajectory average of mutual information $I(A : B)$ between two $L/8$ antipodal segments A and B . The crossing of $I(A : B)$ indicates the critical measurement rate at $\gamma_c \approx 0.2$.

In the main text, we have demonstrated trajectory averaging of classical entropy $\overline{S_{cl}[\{\langle n_i \rangle\}]}$ provides an upper bound on entanglement entropy S_A and is itself bounded by classical entropy of averaged particle number $S_{cl}[\{\overline{\langle n_i \rangle}\}]$. We have displayed the behaviors of $S_{cl}[\{\overline{\langle n_i \rangle}\}]$ in the main text.

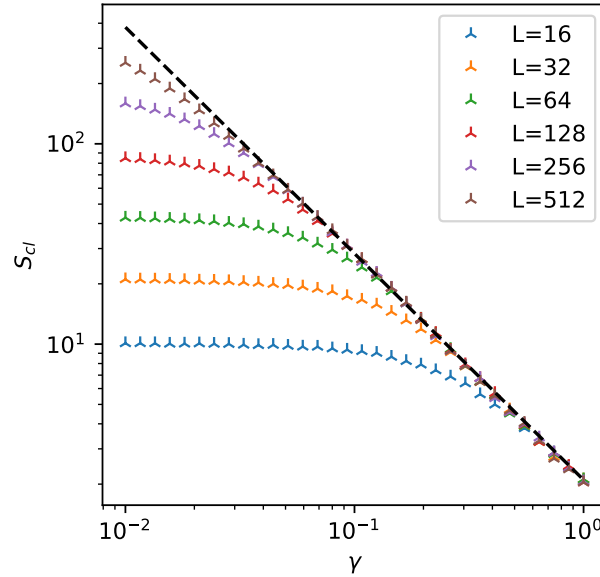


FIG. S5. Trajectory average of classical entropy for systems in different sizes.

Fig. S5 shows that $\overline{S_{cl}[\{\langle n_i \rangle\}]}$ behaves similar as $S_{cl}[\{\overline{\langle n_i \rangle}\}]$ but with slightly different slop, indicating an asymptotic form:

$$\overline{S_{cl}[\{\langle n_i \rangle\}]} \simeq \frac{2.1}{\gamma^{1.13}} \quad (\text{S3})$$

instead of $S_{cl}[\{\overline{\langle n_i \rangle}\}] \sim \gamma^{-1}$. That is, the asymptotic behavior of the trajectory-averaged classical entropy imposes a tighter bound on the steady-state entanglement entropy.

Appendix 5: Numerical simulations of interacted monitoring dynamics

In this section, we provide numerical evidence that the interacting spin system with the Hamiltonian

$$H = \sum_i [J_1(\sigma_i^x \sigma_{i+1}^x + \sigma_i^y \sigma_{i+1}^y) + J_z \sigma_i^z \sigma_{i+1}^z + J_2(\sigma_i^x \sigma_{i+2}^x + \sigma_i^y \sigma_{i+2}^y)], \quad (\text{S1})$$

and subjected to the generalized monitoring described by the operator

$$L_i = \frac{1}{2} S_{i+1}^z (\sigma_i^+ - i \sigma_{i+1}^+) (\sigma_i^- + i \sigma_{i+1}^-) \quad (\text{S2})$$

displays a typical measurement-induced entanglement transition under periodic boundary conditions.

We demonstrate this transition using finite-size exact diagonalization. We remark here that the appearance of an entanglement transition can be better revealed from the mutual information $I(A : B)$ shared by two antipodal sites A and B . This numerical technique has been used, for example, in Refs. [4, 91].

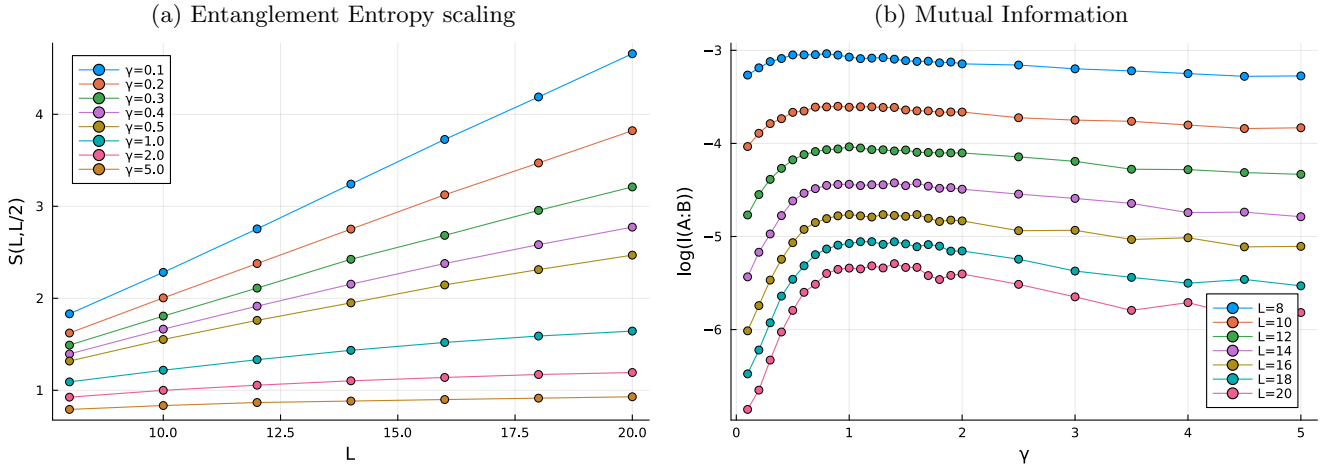


FIG. S6. Exact diagonalization simulation of the entanglement dynamics for systems with $J_1 = J_z = 0.5$, $J_2 = 0.1$, and under periodic boundary conditions. (a) Trajectory average of entanglement entropy for different measurement rates. (b) Trajectory average of mutual information $I(A : B)$ between two antipodal sites A and B . The peak of $I(A : B)$ indicates the critical measurement rate at $\gamma_c \approx 1$.

In Fig. S6a, we first demonstrate that for small γ , the finite size scaling of entanglement entropy $S(L, L/2)$ shows a linear growth in the size L . In the large γ regime, the entanglement is greatly suppressed, suggesting steady states being area-law entangled. To better demonstrate the existence of an entanglement transition, Fig. S6b displays the mutual information $I(A : B)$. The peak in $I(A : B)$ shows near $\gamma = 1$. Due to the finite size available to the numerical simulation, we are unable to pinpoint the critical measurement rate γ_c .

Appendix 6: Monitored free fermion with different conditional feedback

In this appendix, we provide more numerical results on the monitored free fermion system with Hamiltonian

$$H = \sum_i (c_i^\dagger c_{i+1} + c_{i+1}^\dagger c_i) \quad (\text{S1})$$

and the generalized monitoring described by the operator

$$L_i = \frac{1}{2} e^{i\theta n_{i+1}} (c_i^\dagger - i c_{i+1}^\dagger) (c_i + i c_{i+1}). \quad (\text{S2})$$

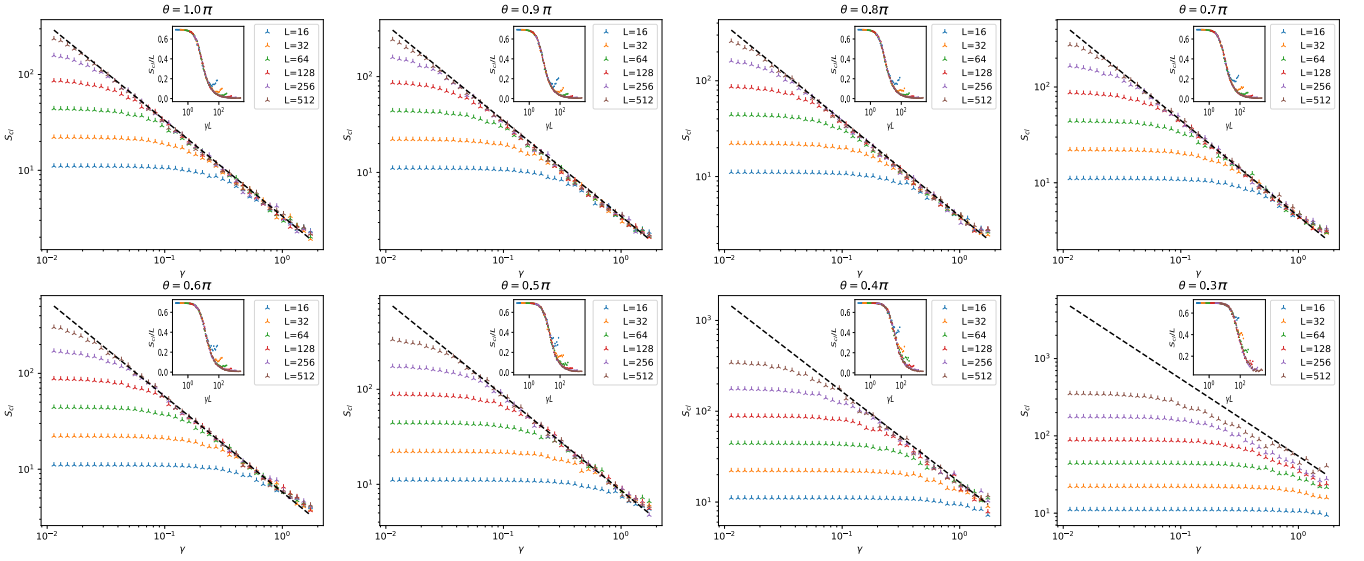


FIG. S7. Steady-state classical entropies $S_{\text{cl}}[\overline{\langle n_i \rangle}]$ for feedback $U_i = \exp(i\theta n_{i+1})$, where we chose θ from π to 0.3π . The data points all approach the asymptotic line $\log \gamma + \log S_{\text{cl}} = c(\theta)$ in the thermodynamic limit. Insets: the data collapse into the form Eq. (S4) for $\gamma < 1$. For $\gamma > 1$, the data points will deviate from the scaling curve.

Apart from the $\theta = \pi$ discussed in the main text, in Fig. S7, we show the numerical simulations on different θ 's. The steady-state classical entropies in the thermodynamic limit $L \rightarrow \infty$ all satisfy the general asymptotic behaviors:

$$S_{\text{cl}}(\gamma, L \rightarrow \infty) = \frac{c(\theta)}{\gamma}, \quad (\text{S3})$$

while the constant $c(\theta)$ increases as θ decreases:

θ/π	1	0.9	0.8	0.7	0.6	0.5	0.4	0.3
$\log c(\theta)$	1.2	1.25	1.35	1.5	1.75	2.15	2.8	4.0

As discussed in the main text, the constant $c(\theta)$ determines the spatial extents of the domain wall. The finite data point we obtained implies that $c(\theta)$ increases exponentially fast when $\theta \rightarrow 0$. In the $\theta = 0$ case, $c(\theta)$ diverges and there is no skin effect. The large-size domain walls impose significant overhead for numerical simulations. For small θ ($\leq 0.3\pi$), accessing the thermodynamic limit becomes practically hard.

However, from the insets of Fig. S7, we see that the numerical data ($\gamma < 1$) for different θ 's all collapse into the scaling form

$$S_{\text{cl}} = Lf_{\theta}(\gamma L), \quad (\text{S4})$$

with the specific scaling function depending on θ . As discussed, Eq. (S4) directly implies the skin effect. Based on the numerical results, we speculate the scaling form Eq. (S4) holds for different θ and γ . Therefore the skin effect is not a fine-tuned property of the feedback parameters.

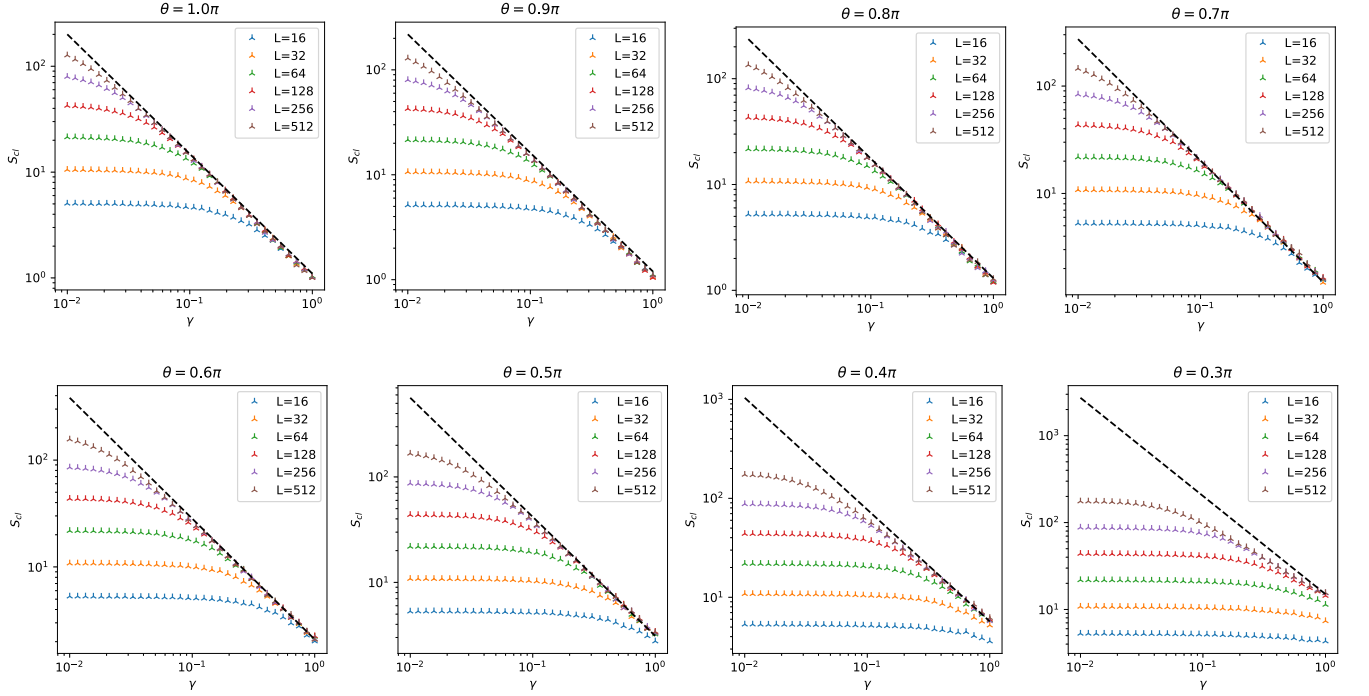


FIG. S8. Steady-state classical entropies $\overline{S_{\text{cl}}[\langle n_i \rangle]}$ for feedback $U_i = \exp(i\theta n_{i+1})$, where we chose θ from π to 0.3π . the data points all approach the asymptotic line $\nu \log \gamma + \log S_{\text{cl}} = c'(\theta)$ where $\nu \approx 1.13$ in the thermodynamic limit.

In Fig. S8, we show the trajectory-averaged classical entropy, which follows similar asymptotic behavior:

$$\overline{S_{\text{cl}}[\langle n_i \rangle]} = \frac{c'(\theta)}{\gamma^{1.13}}, \quad (\text{S5})$$

The constant $c'(\theta)$ increases as θ decreases:

θ/π	1	0.9	0.8	0.7	0.6	0.5	0.4	0.3
$\log c'(\theta)$	0.75	0.85	0.95	1.1	1.4	1.9	2.6	3.4

Appendix 7: Additional generalized monitored model

This section presents an additional generalized monitored model closely related to that we investigate in the main text. Firstly, we expect that the skin effect appears for the system with the same Hamiltonian

$$H = \sum_i (c_i^\dagger c_{i+1} + c_{i+1}^\dagger c_i), \quad (\text{S1})$$

but under the generalized monitoring described by the projector

$$P_{2i-1} = \frac{1}{2}(c_{2i-1}^\dagger - ic_{2i}^\dagger)(c_{2i-1} + ic_{2i}) \quad \text{followed by feedback} \quad U_{2i-1} = e^{i\pi n_{2i}}. \quad (\text{S2})$$

This model is basically the same as the model in the main text, but the number monitoring is reduced by half, and now the projectors $\{U_{2i-1}\}$ all commute with one another. Because of the monitoring, the unit cell is now enlarged by factor 2. Now we apply a unitary transformation to the fermion basis:

$$d_{2i-1} = \frac{1}{\sqrt{2}}(c_{2i-1} + ic_{2i}), \quad d_{2i} = \frac{1}{\sqrt{2}}(c_{2i} + ic_{2i-1}). \quad (\text{S3})$$

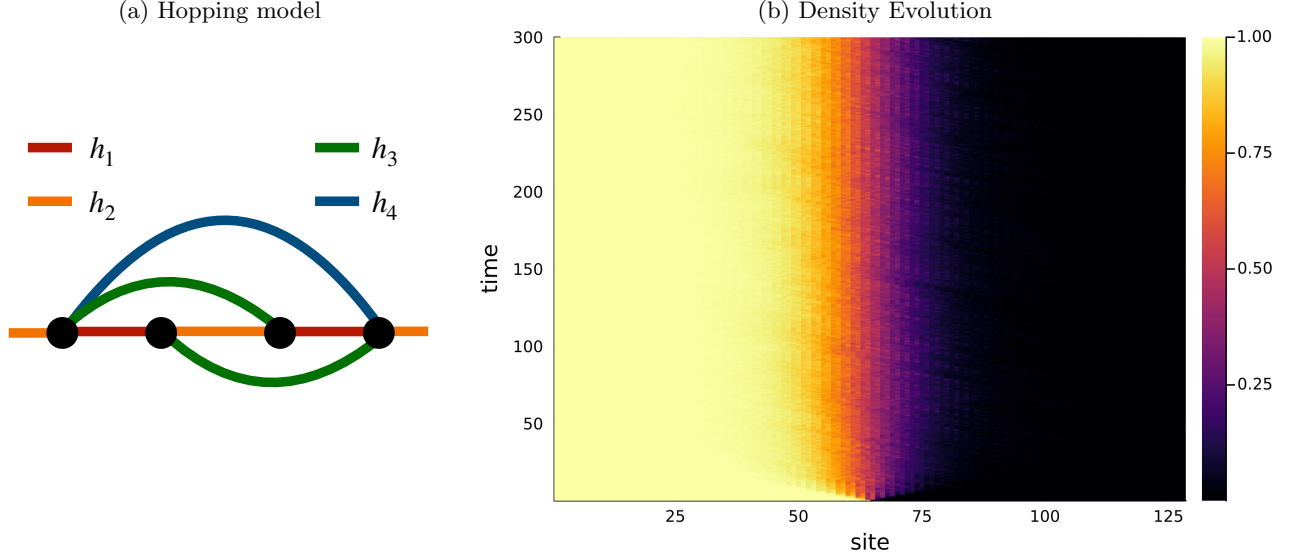


FIG. S9. (a) Hopping model in Eqs. (S4), where lines in different colors represent different hopping terms. (b) Averaged density evolution of particle density for $L = 128$ system under measurement rate $\gamma = 0.3$, and with a SWAP-gate feedback.

The nearest-neighbor hopping Hamiltonian then becomes a more complicated, but still local hopping free fermion model $H = h_1 + h_2 + h_3 + h_4$, where $\{h_1, h_2, h_3, h_4\}$ are hopping terms among neighboring unit cells:

$$\begin{aligned}
 h_1 &= \sum_i (d_{2i-1}^\dagger d_{2i} + d_{2i}^\dagger d_{2i-1}), \\
 h_2 &= \frac{1}{2} \sum_i (d_{2i}^\dagger d_{2i+1} + d_{2i+1}^\dagger d_{2i}), \\
 h_3 &= \frac{i}{2} \sum_i (d_{2i-1}^\dagger d_{2i+1} - d_{2i+1}^\dagger d_{2i-1} - d_{2i}^\dagger d_{2i+2} + d_{2i+2}^\dagger d_{2i}), \\
 h_4 &= \frac{1}{2} \sum_i (d_{2i-1}^\dagger d_{2i+2} + d_{2i+2}^\dagger d_{2i-1}).
 \end{aligned} \tag{S4}$$

The hopping model is depicted by Fig. S9(a), which is invariant under 2-site translation. We note that a particle located on the odd site will be right-moving while a particle located on the even site will be left-moving.

Under the new basis, the projector becomes an onsite measurement of particle occupation on the odd sites:

$$P_i = d_{2i-1}^\dagger d_{2i-1}. \tag{S5}$$

The original feedback operation U_i in this new basis will be rather complicated:

$$U_i = \exp \left[i \frac{\pi}{2} (d_{2i}^\dagger + i d_{2i-1}^\dagger) (d_{2i} - i d_{2i-1}) \right]. \tag{S6}$$

However, as argued in the main text, the specific form of feedback is usually not essential for the skin effect. In this model, we can, for example, choose the U_i as the swap gate

$$U_i = \text{SWAP}_{2i-1, 2i}. \tag{S7}$$

In Fig. S9(b), we plot the density evolution for this model, with SWAP-gate as the the conditional feedback. The numerics shows such system still features a feedback-induced skin effect.

Appendix 8: Measured Floquet circuit model displaying skin effect

8.1. Wave packet motion under Floquet evolution

In this section, we provide examples of the feedback-induced skin effect in the measured quantum circuit. The notion of discrete quantum circuits naturally appears when we use the Trotter decomposition. In general, when a local Hamiltonian can be decomposed into several groups:

$$H = \sum_{\alpha=1}^l H_{\alpha}, \quad H_{\alpha} = \sum_i o_{\alpha,i}, \quad (\text{S1})$$

where each $o_{\alpha,i}$ is a local operator. Within each group, the local operators do not overlap. The time evolution can then be approximated by

$$U(t = N\Delta t) \approx (e^{-iH_1\Delta t} e^{-iH_2\Delta t} \dots e^{-H_l\Delta t})^N. \quad (\text{S2})$$

The decomposition approaches the real dynamics in the $\Delta t \rightarrow 0$ limit. While for practical reason, Δt is a finite value, therefore the dynamics described by Eq. (S2) is a Floquet dynamics with period $T = l\Delta t$.

We show that the notion of wave packet motion is also valid in the context of the Floquet circuit even when the Δt is not vanishing small, as long as the discrete translational symmetry is preserved. For simplicity, we assume that the Floquet circuit has 2-site translational symmetry. We can group two lattice sites into a unit cell and label them as the internal degrees of freedom $a = 1, 2$. The plane wave is then

$$|k, a\rangle \equiv \frac{1}{\sqrt{L}} \sum_j c_{j,a}^{\dagger} e^{-ikj} |0\rangle. \quad (\text{S3})$$

Due to the translational invariance, the evolution $U(T)$ is blocked-diagonal in the momentum space:

$$U_{ab} \equiv \langle k, a | U(T) | k, b \rangle = V(k) \begin{bmatrix} e^{-iE_+(k)T} & 0 \\ 0 & e^{-iE_-(k)T} \end{bmatrix} V(k)^{\dagger}. \quad (\text{S4})$$

The values $E_{\pm}(k)$ extracted from the eigenvalues of U_{ab} are the quasi-energies of the Floquet dynamics. Consider the branch with quasi-energy E_+ . The wave packet with averaged momentum k and averaged position x has the form

$$|k, x; +\rangle \equiv \int \frac{dp}{2\pi} e^{-\alpha(p-k)^2 - ix(p-k)} |p, +\rangle, \quad (\text{S5})$$

where α controls the variance of the momentum distribution of the wave packet. After one period T , the wave packet evolves to

$$\begin{aligned} U(T) |k, x; +\rangle &= \int \frac{dp}{2\pi} e^{-\alpha(p-k)^2 - ix(p-k) - iE_+(p)T} |p, +\rangle \\ &= e^{-iE_+(k)T} \int \frac{dp}{2\pi} e^{-\alpha(p-k)^2 - ix(p-k) - i[E_+(p) - E_+(k)]T} |p, +\rangle \\ &\propto \int \frac{dp}{2\pi} e^{-\alpha(p-k)^2 - i\left[x + \frac{E_+(p) - E_+(k)}{p-k} T\right](p-k)} |p, +\rangle \end{aligned} \quad (\text{S6})$$

Specifically, when α is large, most p will be close to k , and the movement of the averaged position is approximated by

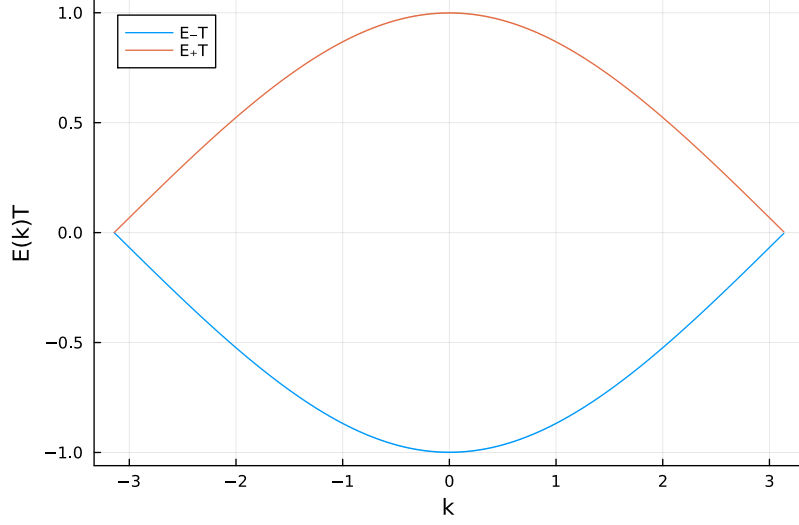
$$x \rightarrow x' \approx x + E'_+(k)T. \quad (\text{S7})$$

We therefore restore the wave packet moving picture in the Hamiltonian dynamics, at least for the nearly monochromatic wave packets.

With the picture in mind, we first consider the Floquet dynamics described by the circuits

$$U(T) = \prod_j \exp \left[-i \left(c_{2j}^{\dagger} c_{2j+1} + c_{2j+1}^{\dagger} c_{2j} \right) T \right] \prod_j \exp \left[-i \left(c_{2j-1}^{\dagger} c_{2j} + c_{2j}^{\dagger} c_{2j-1} \right) T \right] \quad (\text{S8})$$

We can choose an arbitrary finite value of T , say $T = 0.5$. The dispersion is then calculated and displayed in the following:



Note that at the maximal velocity point $k = \pi$, the eigenvectors are

$$\begin{aligned} |\pi, -\rangle &\approx 0.842|\pi, 1\rangle + (0.290 - 0.455i)|\pi, 2\rangle, \\ |\pi, +\rangle &\approx (0.290 + 0.455i)|\pi, 1\rangle - 0.842|\pi, 2\rangle. \end{aligned} \quad (\text{S9})$$

We remark that for finite T , the eigenvectors have shifted compared to the Hamiltonian case. However, the tendency remains the same. That is, the configuration $d^\dagger|0\rangle$ still has a bigger overlap with the right-moving wave packet than with the left-moving ones. We therefore expect that the feedback-induced skin effect still appears in the Floquet model.

8.2. Measurement dynamics

Besides the generalization to the Floquet circuit, we show here that the continuous monitoring setup can be replaced with randomly applying strong projective measurement followed by conditional feedback.

Consider the circuit dynamics in Fig. S10a, where the U_1 and U_2 come from the Floquet dynamics. Under the Jordan-Wigner transformation, they become

$$U_1 = U_2 = \exp\left(-i\frac{T}{2}\sigma_x \otimes \sigma_x\right) \exp\left(-i\frac{T}{2}\sigma_y \otimes \sigma_y\right), \quad (\text{S10})$$

and the measurements are the projective measurement of the observable

$$P_i = \frac{1}{4} (\sigma_i^z + \sigma_{i+1}^z + \sigma_i^x \sigma_{i+1}^y - \sigma_i^y \sigma_{i+1}^x + 2), \quad (\text{S11})$$

followed by the conditional feedback

$$Z = \begin{bmatrix} 1 & 0 \\ 0 & -1 \end{bmatrix}. \quad (\text{S12})$$

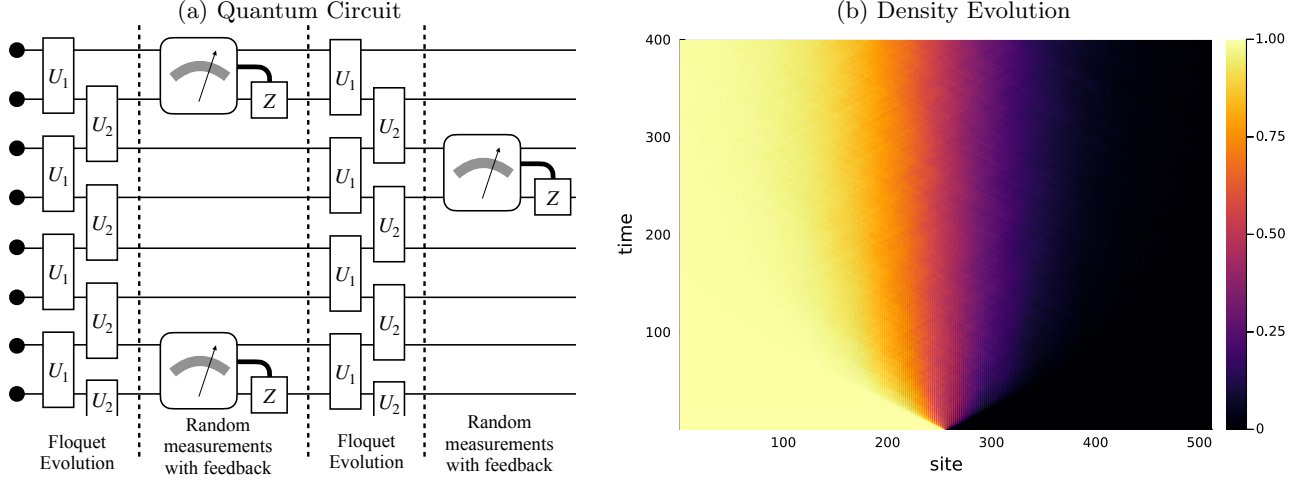


FIG. S10. (a) Quantum circuit model with Floquet circuit evolution and conditional feedback. (b) Density evolution of the measured Floquet dynamics ($L = 512$, $p = 0.02$).

As displayed in Fig. S10b, for a small measurement rate ($p = 0.02$), the feedback still induces the skin effect.

Appendix 9: Experimental proposal on the trapped ions quantum computers

The trapped ions systems [81–84] are one of the ideal platforms to realize medium-scale quantum computation and quantum simulations. Using the $^{171}\text{Yb}^+$ ions trapped by the high-frequency electromagnetic field [81] with fine-tuned laser pulse, the platform is able to:

1. initiate the state as $|0 \cdots 0\rangle$.
2. implement any single-site rotation, which enables to initiate the state to any product state.
3. implement an ‘‘Ising’’ spin-spin interaction [85, 86]: $\text{XX}_{i,j}(\theta) = \exp(-i\theta\sigma_i^x \otimes \sigma_j^x)$.
4. do onsite measurement on σ^z , collapsing qubit to $|0\rangle$ or $|1\rangle$ state.

We remark that, using the combination of single-site and two-site unitary gates, it is possible to realize the YY and XY gates as:

$$\begin{aligned} \text{XY}_{i,j}(\theta) &= \exp(-i\theta\sigma_i^x \sigma_j^y) = \exp\left(-i\frac{\pi}{2}\sigma_j^z\right) \text{XX}_{i,j}(\theta) \exp\left(i\frac{\pi}{2}\sigma_j^z\right), \\ \text{YY}_{i,j}(\theta) &= \exp(-i\theta\sigma_i^y \sigma_j^y) = \exp\left(-i\frac{\pi}{2}\sigma_i^z\right) \exp\left(-i\frac{\pi}{2}\sigma_j^z\right) \text{XX}_{i,j}(\theta) \exp\left(i\frac{\pi}{2}\sigma_i^z\right) \exp\left(i\frac{\pi}{2}\sigma_j^z\right). \end{aligned} \quad (\text{S1})$$

Now consider the monitored circuit model displayed in Fig. S11a, where the Floquet dynamics is the Trotterized version of Hamiltonian (S4). The unitary gates are:

$$U_1 = \text{XX}(\theta) \otimes \text{YY}(\theta), \quad (\text{S2})$$

$$U_2 = \text{XX}\left(\frac{\theta}{2}\right) \otimes \text{YY}\left(\frac{\theta}{2}\right), \quad (\text{S3})$$

$$U_3 = \text{XY}\left(\frac{\theta}{2}\right) \otimes \text{YX}\left(-\frac{\theta}{2}\right), \quad (\text{S4})$$

$$U_4 = \text{XY}\left(-\frac{\theta}{2}\right) \otimes \text{YX}\left(\frac{\theta}{2}\right), \quad (\text{S5})$$

$$U_5 = \text{XX}\left(\frac{\theta}{2}\right) \otimes \text{YY}\left(\frac{\theta}{2}\right). \quad (\text{S6})$$

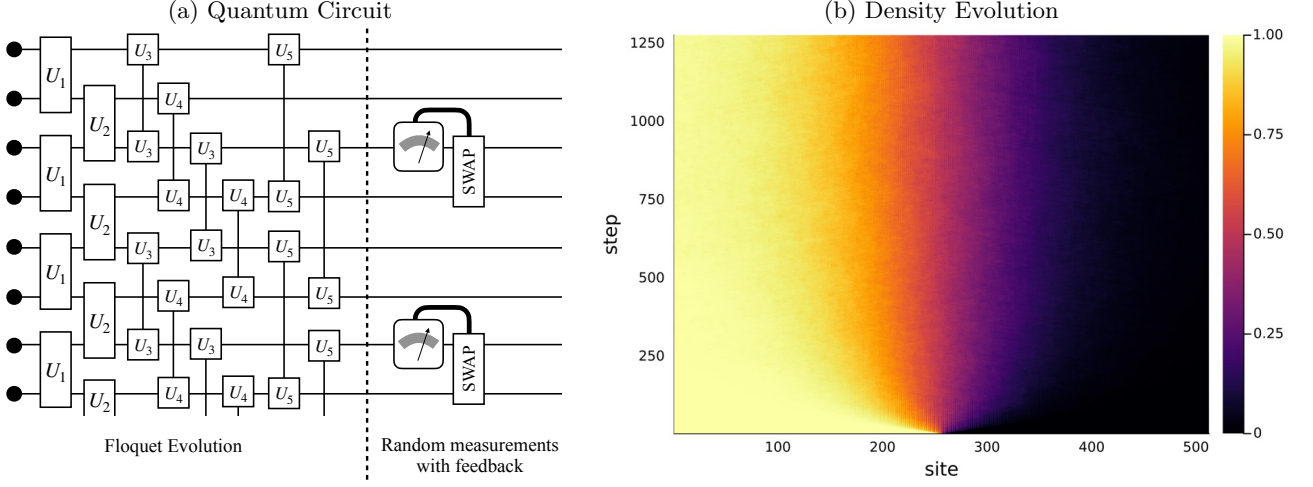


FIG. S11. (a) Quantum circuit of the Floquet monitored dynamics. The unitary gates $U_1 \cdots U_5$ are $XX(\theta)$, $YY(\theta)$, or $XY(\theta)$ gates. In each round of evolution, the system first goes through a Floquet unitary transformation, then subject to projective measurement on randomly chosen (odd) sites. If the measurement result is 1, then a SWAP gate will be applied. (b) Simulation of density dynamics, where $L = 512$, $\theta = \pi/4$, and $p = 0.05$.

The measurement that needs to perform the simple S^z measurement, followed by a conditional swap operation, which is

$$U_{\text{SWAP}} \propto XX\left(\frac{\pi}{4}\right) \otimes YY\left(\frac{\pi}{4}\right). \quad (\text{S7})$$

In Fig. S11b, we simulate the dynamics on a 512-qubit chain, and choose $\theta = \pi/4$, with measurement probability $p = 0.05$. We see the late time state show a clear feedback-induced skin effect.